A Lagrangian perspective on tropical anvil cloud lifecycle in present and future climate

Blaž Gasparini[1], Philip J. Rasch[2], Dennis L. Hartmann[1], Casey J. Wall[3], Marina Dütsch[1]

[1]University of Washington, Seattle, Washington, USA
[2]Pacific Northwest National Laboratory, Richland, Washington, USA
[3]Scripps Institution of Oceanography, University of California San Diego, USA

Key Points:

- E3SM successfully simulates mesoscale convective systems in the Tropical Western Pacific.
- Lagrangian ice crystal trajectories reveal anvil cloud lifetime of 15 hours in both present and future warmer climate.
- Thick anvil clouds contain more ice and have a larger optical depth in a warmer climate, while thin anvil clouds do not change substantially.

Corresponding author: Blaž Gasparini, `blazg@uw.edu`

Abstract

The evolution of tropical anvil clouds from their origin in deep convective cores to their slow decay determines the climatic effects of clouds in tropical convective regions. Despite the relevance of anvil clouds for climate and responses of clouds to global warming, processes dominating their evolution are not well understood. Currently available observational data reveal instantaneous snapshots of anvil cloud properties, but cannot provide a process-based perspective on anvil evolution. We therefore conduct simulations with the high resolution version of the Exascale Earth System Model in which we track mesoscale convective systems over the Tropical Western Pacific and compute trajectories that follow ice crystals detrained from peaks of convective activity. With this approach we gain new insight into the anvil cloud evolution both in present day and future climate.

Comparison with geostationary satellite data shows that the model is able to simulate maritime mesoscale convective systems reasonably well. Trajectory results indicate that anvil cloud lifetime is about 15 hours with no significant difference in a warmer climate. The anvil cloud ice water content is larger in a warmer climate due to a larger source of ice by detrainment and larger depositional growth leading to a more negative net cloud radiative effect along detrained trajectories. However, the increases in sources are counteracted by increases in sinks of ice, particularly snow formation and sedimentation. Furthermore, we find that the mean anvil cloud feedback along trajectories is positive and consistent with results from more traditional cloud feedback calculation methods.

Plain Language Summary

Clouds can have both a cooling and warming effect on climate. Storm clouds in the tropics preferentially cool the climate as they reflect a large fraction of sunlight back to space. Remains of storm clouds, also known as anvil clouds due to their typical shape, reside at very high altitudes and can persist for many hours after the initial intense rain events and extend over vast regions. They keep part of the terrestrial radiation within the atmosphere and therefore warm the climate, similarly to greenhouse gases. The transition from a very reflective storm cloud to a thin anvil cloud is not yet well understood despite playing an important role for tropical climate. We study such transitions with the help of climate model simulations in which we follow ice crystals from their origin in storm clouds as they develop into thin anvil clouds and eventually disappear. The climate model allows us to study this process both in present-day as well as a warmer future climate. We find that in a warmer climate the storm clouds contain more ice and reflect more sunlight, which leads to more cooling, while the thin anvil clouds do not change much with warming.

1 Introduction

Tropical cloud radiative effects (CRE) are determined by the relative proportions of thick, freshly detrained anvil clouds, and the thin anvils they evolve into. For thick anvil clouds, shortwave (SW) effects prevail over longwave (LW) effects, leading to a net climatic cooling effect. In contrast, LW effects prevail for thin anvil clouds with cloud optical depth (COD) smaller than 4, leading to a net warming effect (Kubar et al., 2007; Berry & Mace, 2014; Hartmann & Berry, 2017). Thick anvils occur adjacent to deep convective towers and form a reflective cold cloud shield. While most of the detrained ice that forms fresh anvils is removed from the atmosphere within a few hours, thinning anvil clouds persist for much longer, often extending for hundreds of kilometers beyond the areas of active convection (Mapes & Houze, 1993; Mace et al., 2006; Protopapadaki et al., 2017). Any response of anvil cloud properties (e.g. occurrence, extent, or lifetime) to global warming could therefore lead to a significant radiative feedback.

The tropical troposphere is to first order controlled by an interplay between radiative cooling from the emission of thermal radiation by water vapor and latent heating in convective updrafts. The peak of convective detrainment therefore occurs just below the altitude where the radiative cooling becomes inefficient, at a temperature of about 220 K. This relation will not change in a warmer climate with anvil clouds shifting to higher altitudes while remaining at a "fixed" temperature as proposed by the "fixed anvil temperature" (FAT) hypothesis (Hartmann & Larson, 2002). FAT has since been refined to take into account small cloud temperature changes associated with the presence of ozone, well-mixed greenhouse gases or changes in relative humidity (Zelinka & Hartmann, 2010; Harrop & Hartmann, 2012). It has been confirmed by cloud resolving model (CRM) and general circulation model (GCM) studies studies (Kuang & Hartmann, 2007; Harrop & Hartmann, 2016; Hartmann et al., 2019; Boucher et al., 2013; Zelinka et al., 2016), and satellite observations (Zhou et al., 2014; Marvel et al., 2015; Norris et al., 2016; Mace & Berry, 2017).

Several modeling studies showed a decrease in high cloud fraction with increased sea surface temperatures (SSTs) (Tompkins & Craig, 1999; Zelinka & Hartmann, 2010; Khairoutdinov & Emanuel, 2013). Bony et al. (2016) proposed a thermodynamic mechanism connecting the decrease in cloud fraction to increases in static stability. The mechanism involves FAT, static stability, and the reduction of convective outflow (and thus anvil cloud fraction) in a warmer world. The upper tropospheric static stability is bound to the moist adiabatic lapse rate. As the troposphere expands, the decrease in pressure leads to an increased saturation specific humidity at a fixed temperature, which consequently warms the upper troposphere and increases its static stability (Zelinka & Hartmann, 2010; Hartmann et al., 2020). Consequently, based on the FAT hypothesis, a higher stability leads to a smaller convective detrainment, reducing the anvil cloud fraction and therefore limiting the tropical high cloud positive feedback.

Despite the arguments above that high cloud fraction should decrease in a warmer Earth, preliminary results from the Radiative-Convective Equilibrium Modeling Intercomparison Project show a large spread of modeled responses to increases in SSTs (Wing et al., 2019) including anvil cloud fraction changes. Moreover, various versions of the NICAM global and limited area CRM that represent convective cloud procesess using fewer parameterizations than GCMs (and thus may be more realistic) show an increase in tropical high clouds with global warming (Satoh et al., 2011; Tsushima et al., 2015; Ohno et al., 2019), intensifying the already positive high cloud altitude feedback. If the mechanism proposed by Bony et al. (2016) is present, an increase in high cloud fraction with warming simulated by some models implies that additional unknown feedbacks should play an important role. Ohno and Satoh (2018) showed that high cloud feedbacks depend upon changes in atmospheric cloud radiative effects (ACRE) and their effect on cloud-scale circulations, which can modulate the ice source and sink processes, particularly deposition and ice crystal sedimentation. Many of these processes are represented crudely in today's models, and Ohno et al. (2019) additionally pointed out the important role of turbulent mixing, which strongly depends on vertical grid spacing.

Several observational studies show that tropical outgoing longwave radiation (OLR) increases with surface warming more than predicted by the Planck response to warming (Lindzen & Choi, 2011; Choi et al., 2017). Lindzen et al. (2001) proposed a controversial hypothesis based on geostationary satellite observations, stating that the coverage of anvil clouds in the tropics will decrease with warming due to increased precipitation efficiency and consequent decreased convective detrainment, allowing a higher OLR. They named it the "Iris effect", after the iris of the human eye, which expands in conditions of weak light to let more light pass, similarly to the putative tropical OLR response to the surface temperature in letting more OLR out in a warmer climate by reducing the high cloud cover. The Iris effect was proposed as a negative climate feedback, counteracting the greenhouse gas warming effect. The work was soon criticized for methodological reasons and lack of a clear physical mechanism (e.g. Fu et al. (2002); Hartmann and Michelsen (2002)). However, the idea has recently gained more interest following the

modeling study of Mauritsen and Stevens (2015) that implemented a temperature-dependent convective autoconversion rate, which resulted in a decreased climate sensitivity.

Hence, our understanding of tropical high clouds and their responses to global warming are highly uncertain, sometimes leading to diametrically different conclusions. The role of specific microphysical processes, their interaction with radiation, and their changes due to surface warming and greenhouse gas increase are still unclear. This study's goal is to provide a better understanding of some of the processes controlling anvil cloud decay and their responses to global warming with the help of a Lagrangian approach in which we track ice crystals detrained from regions of active deep convection. We show that the Lagrangian approach can, coupled to a high resolution model that is skillful in simulations of relevant climatic processes, reveal a process based view on the evolution of high clouds and their responses to global warming that is complementary to the standard climate model analysis.

1.1 Lagrangian perspective on anvil evolution

Atmospheric models can be separated into two categories based on their treatment of fields' evolution related to the wind flow. Eulerian models treat the field evolution as a function of fixed space coordinates and time. In contrast, Lagrangian models describe fields following particles or air parcels along the flow. The Lagrangian perspective is particularly useful for studies of dynamic, quickly changing phenomena, giving a natural perspective on air parcel evolution. Lagrangian tracking of detrained clouds and water vapor has provided new insights into the lifecycle of tropical high clouds. For example, Luo and Rossow (2004) found that about 50% of tropical cirrus clouds originate from deep convection. Mace et al. (2006) used a combination of ground-based radar data with satellite feature tracking to show that tropical anvil cloud systems are long-lived with lifetimes of about 12 hours. Gehlot and Quaas (2012) were the first to apply a similar tracking method on GCM model output to verify the model against observations and look at the changes in anvil cloud lifecycle in a simulation with increased SSTs. The Lagrangian analysis suggested that a combination of increased cloud fraction and cloud altitude was the driving force behind a positive cloud feedback, despite increases in cloud albedo. Jensen et al. (2018) followed trajectories of ice crystals detrained from a midlatitude thunderstorm driven by a CRM simulation. They simulated the first 3 hours of the microphysical evolution of detrained ice crystals and showed the large importance of gravitational settling and depositional growth for the anvil evolution. So far, three-dimensional Lagrangian tracking has never been applied to studies focusing on deep convective outflow and the transition between deep cumulus to thick and thin anvil clouds. The tracking of detrained air parcels and ice crystals allows us to determine the lifetime of anvil clouds and estimate sources and sinks of ice during the cloud evolution and their changes with global warming.

The study focuses on the region between 130°-180°E and 20°S-20°N, which we call Tropical Western Pacific (TWP) and is typical of regions with warm and uniform SST and frequent deep convection. Only anvil clouds that originate from maritime deep convective cores are considered as the continental/island deep convection is controlled by different processes and is less important for the tropical radiation balance. Section 3.1 briefly assesses the model performance in the TWP. The Lagrangian perspective on the simulated anvil cloud evolution in present climate is presented in Section 3.2. Mean climate responses to warming are presented in Section 4.1, followed by a description of mesoscale convective systems' (MCS) responses to global warming in Section 4.2. Finally, Section 4.3 presents changes of anvil properties along detrained trajectories due to global warming and their radiative implications. A discussion on the implications and limitations of the model simulations is provided in Section 5. Conclusions are given in Section 6.

2 Methods

2.1 Model

We use the Exascale Earth System model (E3SM), a new GCM developed by the US Department of Energy (J. Golaz et al., 2019). The model consists of interacting components simulating atmosphere, land surface, ocean, sea ice and rivers. The atmospheric component of E3SM (Rasch et al., 2019) is a descendant of the CAM5 model (Neale et al., 2012), including new ways of coding, improved model performance, increased resolution, and numerous additional physical parameterizations related to clouds and aerosols. The model uses a spectral finite element dynamical core (Dennis et al., 2012) with 72 vertical layers. The upper tropospheric resolution of about 500 m is significantly higher than most state-of-art GCMs, and allows for a more realistic representation of upper tropospheric clouds. E3SM performs well compared to other CMIP5 models (J. Golaz et al., 2019), despite known model biases (Xie et al., 2018; Y. Zhang et al., 2019). In particular, the model underpredicts clouds in the tropical warm pool area, which was found to be related to the increase of the vertical resolution from 30 to 72 layers (Xie et al., 2018).

We use the high resolution (about 0.25°) version of the model (Caldwell et al., 2019), in which the large tropical MCS are better resolved. E3SM uses a convective parameterization by G. J. Zhang and McFarlane (1995) with the dilute plume closure by Neale et al. (2008). Turbulence, shallow convection and cloud macrophysics are simulated by the third order turbulence closure Cloud Layers Unified By Binormals (CLUBB) parameterization (J.-C. Golaz et al., 2002; Larson & Golaz, 2005). The model uses an updated version of Morrison and Gettelman (2008)'s scheme for stratiform cloud microphysics (Gettelman & Morrison, 2015) and is coupled with the RRTMG radiative transfer model (Mlawer et al., 1997; Iacono et al., 2008). The COSP version 1.4 satellite simulator (Bodas-Salcedo et al., 2011) is run in parallel to the model. The atmospheric component of the model was coupled with the land model only.

2.2 Simulations

We perform two simulations representing present day climate (REF, climREF, see also in Table 1) and two simulations representing a possible warmer future climate state (4K, clim4K). SSTs and sea ice extent were prescribed using a monthly present-day climatology (simulations REF,climREF) based on the Smith/Reynolds EOF dataset (Hurrell et al., 2008). Simulations 4K and clim4K use the same SST pattern assuming a uniform 4K warming. The simulations used for calculation of the mean climatic properties and cloud feedbacks with monthly output frequency (climREF and clim4K) were run for only 3 years due to the large computational expense. The COSP simulator was active only for 1 year out of the 3 simulated years.

The simulations REF, NUDGE, and 4K, used for both MCS tracking and trajectory calculations last 3 months (Jun 1 - Aug 31) with a 7 day spin-up period (Table 1). Because many fields were archived hourly for subsequent analysis, longer simulations were not possible due to storage space limitations. The NUDGE simulation uses a linear interpolation nudging technique developed by Sun et al. (2019). The model horizontal wind fields were nudged at every model timestep to an interpolated value based on 6 hourly ERA-Interim reanalysis data (Dee et al., 2011), with a relaxation timescale of 6 hours. The simulation NUDGE uses monthly mean SSTs for the months of June-August 2016 from the same dataset for a better comparison with MCS observations from the same period.

In addition we estimate cloud feedbacks based on Zelinka et al. (2016), which uses cloud radiative kernels (Zelinka et al., 2012a) and output from the ISCCP satellite simulator (Klein & Jakob, 1999; Webb et al., 2001) separated into cloud top pressure and COD bins. The feedback calculation allows one to separately account for the contribution of changes in cloud altitude, cloud amount, and cloud optical depth to the total cloud

Table 1. A list of performed simulations.

Simulation	Length	Output frequency
NUDGE	3 months	1 hour
REF	3 months	1 hour
4K	3 months	1 hour
climREF	3 years	1 month
clim4K	3 years	1 month

feedback. We calculate both the cloud feedback of all clouds as well as the cloud feedback for clouds with cloud top pressures smaller than 440 hPa.

2.3 CERES satellite data

We use the CERES-derived top-of-atmosphere radiative fluxes (Wielicki et al., 1996) from the CALIPSO-CloudSat-CERES-MODIS (CCCM) data set (Kato et al., 2011) for the months of June-August 2007–2010 in the TWP (20°S to 20°N, 130 to 180°E). The horizontal resolution of CERES pixel data is approximately 30 km. To avoid problems at large solar zenith angles, we limit the analysis to CERES pixels for which the solar zenith angle and the CERES viewing angle zenith are smaller than 40°. Given that the data in the CCCM data set are collocated with the CloudSat-CALIPSO radar-lidar measurements, that limits the observations to the 1.30 pm (afternoon) overpass of the A-Train satellite constellation.

2.4 Geostationary satellite data

We use the Himawari-8 geostationary satellite observations (Bessho et al., 2016) of brightness temperature (BT) at the infrared channel (11.2 μm) between 1 June - 31 August 2016. The downloaded Himawari data product only includes every fourth pixel and scan line, making the effective horizontal resolution about 8 km at nadir and 12 km at the edge of the study domain. These data were subsequently regridded to 0.25° (about 25 km) to match the model output. Regridded pixels were computed by averaging the native grid pixels within the new grid boundaries. The datasets' temporal resolution of 1 hour allows individual MCS to be tracked throughout their lifecycle.

2.5 MCS tracking

We apply an MCS tracking algorithm to the 11.2 μm BT measurements from the Himawari and to the 10.5 μm simulated BT retreival using the COSP satellite simulator. The small difference in the BT wavelength of the two channels does not affect our findings. Both Himawari and E3SM data are tracked in 1 hour intervals, enabling an accurate MCS tracking. The tracking algorithm is based on Fiolleau and Roca (2013) and is described in detail in Wall et al. (2018). It consists of two steps:

1. Detection step: The cold core is detected based on the BT threshold (between 200 and 214 K depending on the specific case - see Tab. 2). The cold core must cover at least 17 pixels and last for at least 2 hours to be considered by the algorithm.
2. Spreading step: The cold cloud mask is incrementally increased from the BT threshold to the warm limit in both space and time (ranging between 235 and 240 K as listed in Tab. 2).

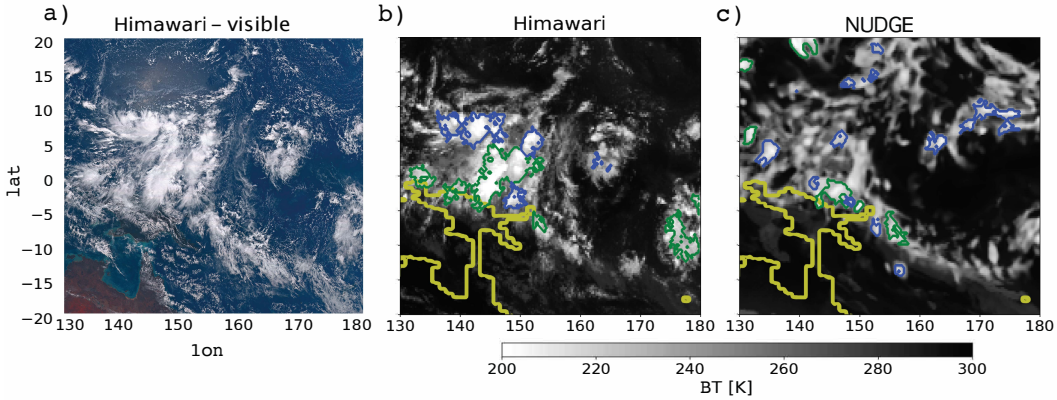

Figure 1. A snapshot of the region of interest. (a) visible Himawari satellite image; (b) the equivalent BT measurement; (c) the NUDGE model simulation at the same timestep. Blue contours represent tracked MCSs, green contours represent MCSs that are tracked but removed from the analysis as they touch the edge of the domain or land. Yellow contours represent boundaries of land masses.

The tracking algorithm is able to track MCS throughout their lifecycle, from the growth to the decay stage (Wall et al., 2018). However, once the clouds become optically thinner, the BT signal of cold clouds is mixed with the signal from warmer, lower lying levels. The algorithm reliably tracks upper tropospheric clouds to a COD of about 3, which corresponds to the warm BT limit of 235-240 K. The algorithm therefore cannot account for the thin anvil clouds that spread beyond the region detected by the cloud mask. An example of the cold cloud mask output of the tracking algorithm is shown in Fig 1 b and c. The blue and green contours outline the limits of the detected cold cloud mask which we take as the MCS boundaries. The green contoured MCSs are removed from the analysis as they either cross land at some point in their lifetime or touch the domain boundaries. The MCS lifetime is defined as the time between the first and last detection of an MCS based on the cold cloud mask.

We use two separate ways of setting the BT threshold for tracking the MCS. The first method relies on fixed BT thresholds of 210 K for cold core detection and 240 K for the warmest contours that are tracked as part of the cold cloud area (see Wall et al. (2018) for details). However, fixed BT thresholds propagate mean climatic errors into the object-oriented MCS tracking analysis. Those errors will be discussed below in the evaluation of BT PDFs in Fig. 3. The work by Rempel et al. (2017) and Senf et al. (2018) suggests that it can also be useful to apply a BT correction before the object-based MCS tracking analysis, so we therefore also use a prescribed lower and upper BT percentile to define the cold cloud mask used to track the detection and spread of cold cloud surface area instead of a fixed BT limit. A percentile-based metric also helps estimating the impacts of global warming driven changes of MCS properties and the anvil cloud evolution, as described in Sections 4.2 and 4.3. Similar percentile based comparison metrics are frequently used in studies of extreme precipitation responses to global warming (Fischer & Knutti, 2015, 2016; Pendergrass & Knutti, 2018).

We chose the 0.4 and 8.15 BT percentiles as the cold core detection limit and the upper BT limit, which correspond to the BT values of 200 K and 235 K in the full resolution Himawari dataset for consistency with the work by Wall et al. (2018). The chosen lower percentile limit corresponds to a BT of 201.4 K in the regridded Himawari dataset used in this analysis, to 210 K in the nudged, and 213.5 K in the free running E3SM model simulation as stated in Table 2.

2.6 Lagrangian tracking of anvil clouds

2.6.1 Determination of trajectory starting locations

High frequency (1 hour) model output from June 1 to August 31 from simulations REF and 4K is used for calculating forward trajectories. The forward trajectory calculation is designed to monitor and capture the decay of anvil clouds from their early thick stage until dissipation as thin cirrus. Monitoring starts at the peak of MCS convective activity, defined as the point in the MCS evolution when the detected cold cloud mask occupies the largest surface area (Roca et al., 2017). At this point the model columns covered by the cold cloud mask (blue contours in Fig. 1) are selected to determine the right vertical launch level for the trajectories. The vertical launch level is chosen to be the first model level from the model top downward to have an ice water content (IWC) larger than 3 10^{-5} kg kg^{-1} and a detrainment tendency from the parameterized convective updrafts larger than 1 10^{-9} kg kg^{-1} s^{-1}. Launch levels are limited to temperatures colder than -35°C, as the study is focused on cold portions of anvil clouds.

2.6.2 Trajectory calculation

Trajectories are computed in a post processing step with the Lagrangian Analysis Tool (LAGRANTO) (Wernli & Davies, 1997; Sprenger & Wernli, 2015). Trajectories are computed forward in time for 40 hours. Microphysical and radiative quantities are traced by identifying the value of those quantities from an archived model dataset followed by a bilinear interpolation of the neighboring grid values in the horizontal dimension (latitude, longitude) and a linear interpolation in the vertical dimension (model level) (Sprenger & Wernli, 2015).

We analyze anvil evolution in two different ways, once neglecting and once including the impact of ice sedimentation on trajectories:

1. Trajectories follow air parcels (NOSEDI): Model calculated large-scale wind fields (U,V,OMEGA) are used to solve the trajectory equation.
2. Trajectories follow ice crystals (SEDI): The model-computed ice crystal mass sedimentation velocity (ICsed) is added to the vertical velocity (ω). The vertical component of the trajectory equation is transformed assuming: $\omega_{trajectory} = \omega_{grid-mean} + ICsed_{grid-mean}$. This allows us to reconstruct pathways of detrained ice crystals and track the changing microphysical and radiative properties along those trajectories after detrainment. The analysis neglects snow particles due to their larger sedimentation velocity that leads to a rapid removal from the atmosphere and therefore a smaller climatic influence compared to the longer lived detrained ice crystals.

In a second post processing step we remove the trajectories that encountered a subsequent significant episode of detrained ice (i.e. detrainment larger than 0.3 10^{-9} kg kg^{-1} s^{-1}) after the initial 4 hours of the development. This allows us to study cloud decay of anvils that are not influenced by new occurrence of convection. The additional criterion reduces the number of selected trajectories by 80%, from a total number of 200000 to about 25000, while not affecting the main conclusions of our study. We define a trajectory as containing "ice cloud" if the local cloud fraction (CLOUD) exceeds 10% and at the same time IWC exceeds 0.1 mg kg^{-1}. The IWC limit was chosen to be close to the minimum detection limit by CALIOP lidar, roughly corresponding to COD of 0.01 (Avery et al., 2012). The anvil cloud lifetime is defined as the point in time when the fraction of trajectories containing cloud drops below 50%. Note that the total column cloud fraction could still be large as air parcels containing ice can be detrained from multiple levels below and above the tracked one. Due to lateral mixing the cloud properties along trajectories in the later stage of anvil evolution represent a mix of air from anvil

and non-anvil air masses. We omit the radiatively active and prognostic snow from the trajectory analysis due to its larger sedimentation velocity compared to cloud ice (Zhao et al., 2017) and storage space limitations.

3 Results - present climate

3.1 Model evaluation

3.1.1 Mean climate in the Tropical Western Pacific

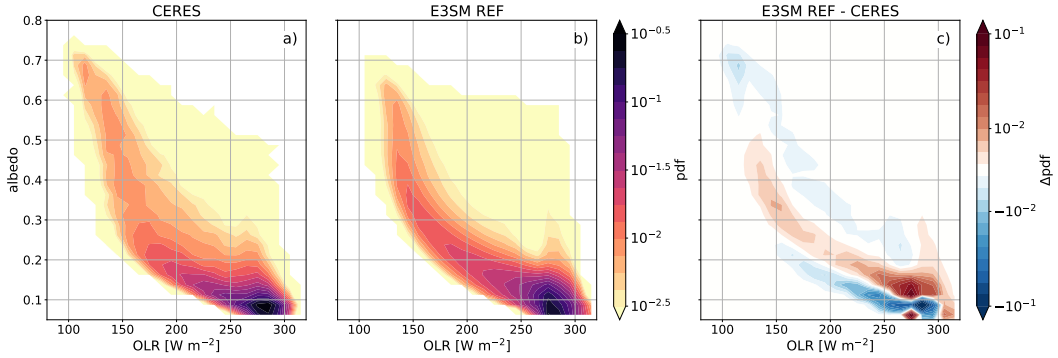

Figure 2. Albedo-OLR histogram for the Tropical Western Pacific from 4 years of CERES radiative flux observations for months June-August (a), the equivalent from the REF model simulation (b), and the anomalies between the two (c).

Figure 2 shows the probability density function (PDF) of OLR-albedo pairings observed by CERES satellite for the months of June-August, similarly to Fig. 2 in Hartmann and Berry (2017), and the equivalent fields simulated by the model. The model output is limited to grid boxes with insolation values exceeding 1000 W m^{-2}, which approximately corresponds to the zenith angle limit of 40° used to filter the CERES data. The general shape of the histogram describes the evolution of anvil clouds: their lifecycle begins in very reflective deep convective cores at low OLR and high albedo values. The detrained anvil clouds gradually thin, decrease their albedo, and allow more OLR to escape to space until reaching the modal point of the distribution at albedo values of about 0.08 and OLR of 270-290 W m^{-2} which corresponds to nearly clear sky conditions. The model is able to reproduce the general shape of the distribution and therefore anvil decay remarkably well, with the exception of the missing highest albedo and lowest OLR points and a minor albedo overestimation at OLR values between 200 and 300 W m^{-2}. E3SM therefore shows good skill in simulating the process of anvil thinning, that is on one hand crucial for the radiative balance of tropical deep convective regions, while on the other hand traditionally challenging for GCMs to correctly simulate (Wall & Hartmann, 2018).

3.1.2 Mesoscale convective systems

Figure 3 shows the PDF of BT in the Tropical Western Pacific region observed by Himawari and modeled by E3SM with the help of a satellite simulator. We focus for now on the NUDGE and REF simulations and refer back to the figures to examine climate change effects in the 4K simulation only in Section 4. The Himawari distribution sharply peaks at about 295 K, while the nudged and free running model simulations show a peak at a few K warmer temperatures. This BT peak corresponds to clear sky regions, clear sky regions with thin cirrus clouds, or regions covered by low clouds. The observed and

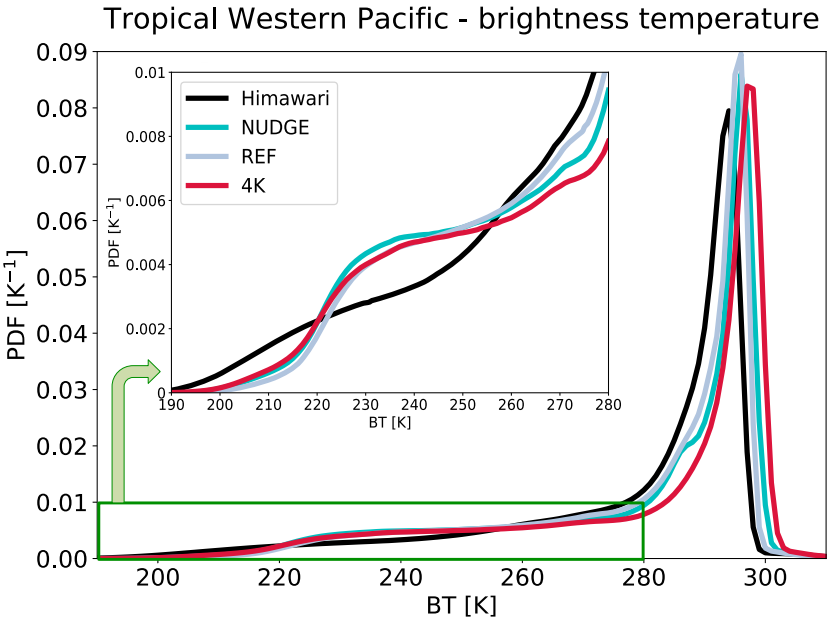

Figure 3. BT histogram for the Tropical Western Pacific in JJA 2016 from Himawari observations and nudged model simulations for Jul 2 2016 at 1.00 GMT.

simulated distributions are negatively skewed with a long tail extending down to 190 K. BT values colder than 240 K correspond to cold cloud tops; we define such gridboxes as cold cloud fraction. These BT values include deep convective cores, and anvil clouds of visible COD greater than about 3, and do not include thin anvil cloud and other in-situ formed cirrus clouds. E3SM simulates a cold cloud coverage of 9.7% in the nudged simulation (NUDGE) and 8.5% in the free running simulation (REF). This is close to the observed value of 9.8 %. The model substantially underestimates the occurrence frequencies of BT colder than 220 K (represented by the highest albedo and lowest OLR values in Fig. 2), and overestimates BT in the range between 225 and 250 K. This is a signal of a too low (and consequently too warm) cloud top, caused by a deep convective detrainment level bias and the underestimation of the strongest overshooting convective cores, as already noted by Y. Zhang et al. (2019). The bias, which existed in the predecessor model CAM5 (Wang & Zhang, 2018), has not been solved in the E3SM model, in spite of increased vertical resolution and efforts to address the bias through tuning (Xie et al., 2018). Qualitatively the biases are also visible by comparing BT snapshots in panels b and c in Fig. 1. Moreover, despite efforts to evaluate the fields at the same nominal resolution, the model lacks the fine structures observed by Himawari. This is not surprising, as the effective model resolution is about 3-4 times larger than a single gridbox cell for the spectral element dynamical core used here.

When MCS are defined using fixed BT thresholds, the model underestimates the number of MCS and overestimates their lifetime (Table 2 and Fig. 4 a,c), while simulating MCS of comparable size. The maximum MCS equivalent diameter is close to 250 km in both Himawari and E3SM. The MCS mean lifetime from Himawari observations is found to be 12.7 hours, which is comparable to Wall et al. (2018). The simulated MCS are more persistent, with average lifetimes of 19 hours (NUDGE) and 17 hours (REF). The excessive lifetime of the model clouds can at least in part be attributed to a series of parameterization choices made in the development of the atmospheric component of E3SM (Rasch et al., 2019). The radius of ice crystals detrained from deep convection was set to 12 μm, which is smaller compared to observations (Van Diedenhoven et al., 2016),

Table 2. Tracked MCS properties. The numbers represent mean values with the respective standard deviations. The median values are in brackets.

	Himawari	**NUDGE**	**REF**	**4K**
1. Fixed BT				
BT limit [K]	210-240	210-240	210-240	210-240
MCS number	1762	1243	853	1354
Lifetime [h]	12.7±5.4 (11)	18.8±6.1 (18)	16.9±5.4 (16)	15.9±5.4 (15)
Equiv. diameter [km]	247±97 (223)	260±75 (248)	267±68 (257)	264±81 (250)
2. Percentile based BT				
BT limit [K]	201.4-238.1	209.9-236.7	213.5-239.3	209.0-237.3
MCS number	794	1234	1285	1178
Lifetime [h]	14.5±5.0 (13.5)	17.9±6.0 (17.0)	16.2±6.0 (15.0)	15.6±5.4 (15.0)
Equiv. diameter [km]	302±90 (290)	247±73 (235)	248±69 (237)	260±80 (246)

in order to increase the amount of cloud ice in the atmosphere (Xie et al., 2018). This choice, in conjunction with a decision to use the Meyers et al. (1992) ice nucleation parameterization (known to produce unrealistically high nucleation rates) in the high resolution version of E3SM (Caldwell et al., 2019) produces too many ice crystals that consequently remain small during vapor deposition. Finally, as mentioned in the previous subsection, the effective model resolution is larger than its nominal resolution. Regridding the Himawari observations to 0.5° and 1° increases the MCS lifetime for 1 and 2 hours, respectively, explaining part of the model bias.

Results using the percentile based masking give a different perspective on simulated MCSs: in this case the model overestimates the MCS number but underestimates the surface area, with a comparable MCS lifetime (Fig. 4 b,d). This is expected, as the percentile-based BT MCS detection threshold of 201.4 K for Himawari observations is significantly lower than 209-213.5 K for the model simulations. MCS with colder BT indicate a stronger convective activity with higher and colder cloud tops. The higher convective activity is also connected to a longer MCS lifetime and larger MCS surface area (Machado et al., 1998; Protopapadaki et al., 2017; Strandgren, 2018).

Figure 5 shows the diurnal cycle of the number of MCS at peak extent in each of the 3-hourly bins. The peak MCS extent was previously shown to correlate with the peak in convective activity and with the lowest BT that is achieved in the course of an MCS lifecycle (Roca et al., 2017). When using a BT threshold of 210 K for the detection of cold cores, the observations show a double peak in MCS activity: the first peak occurs in early morning hours (3-5 local time), the second peak occurs in the afternoon hours (15-17 local time). However, when using the colder percentile-based BT threshold for the detection of cold convective cores, the afternoon peak disappears. This result is consistent with Nesbitt and Zipser (2003) that showed an early morning peak in MCS activity, followed by a weaker afternoon peak of warmer BT features representing weaker deep convection. The model simulates a similar double peak in MCS activity when using the fixed 210 K cold core detection threshold in both the REF and NUDGE simulation. The percentile based model results still show the secondary afternoon peak, which is not surprising, given that the percentile based cold core detection threshold does not change much from a fixed threshold of 210 K.

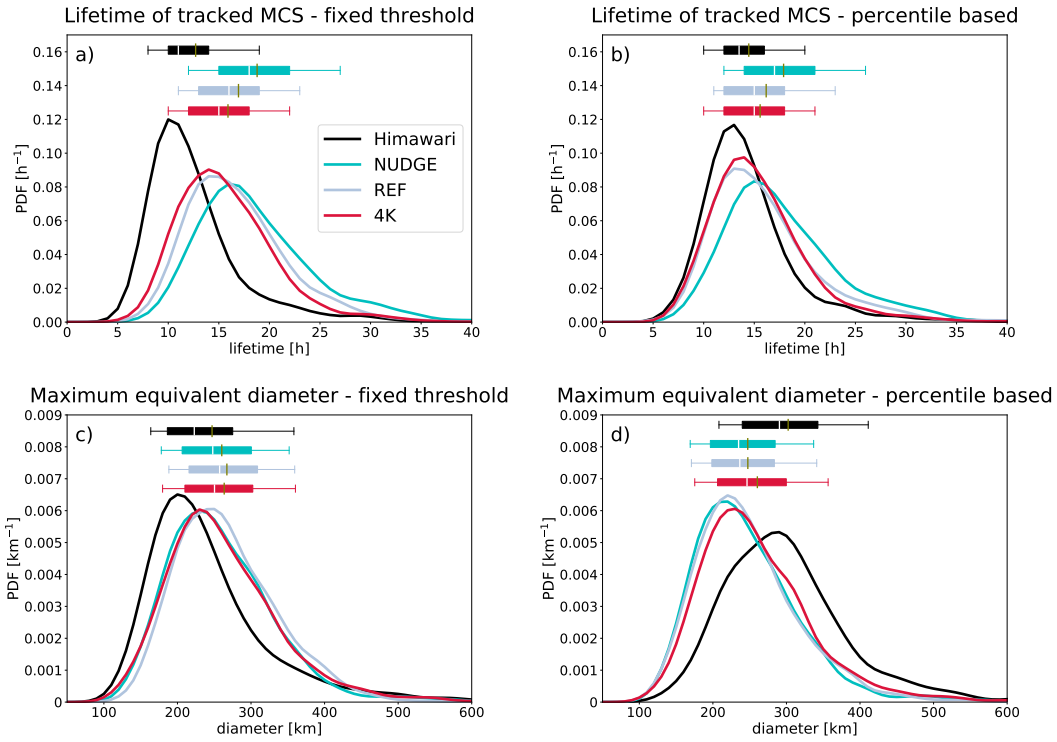

Figure 4. Lifetime and maximum diameter distribution of tracked MCS. The boxplot area is shaded between the 25th and 75th percentiles, while its whiskers represent the 10th and 90th percentiles. The olive lines represent the mean values of the distributions.

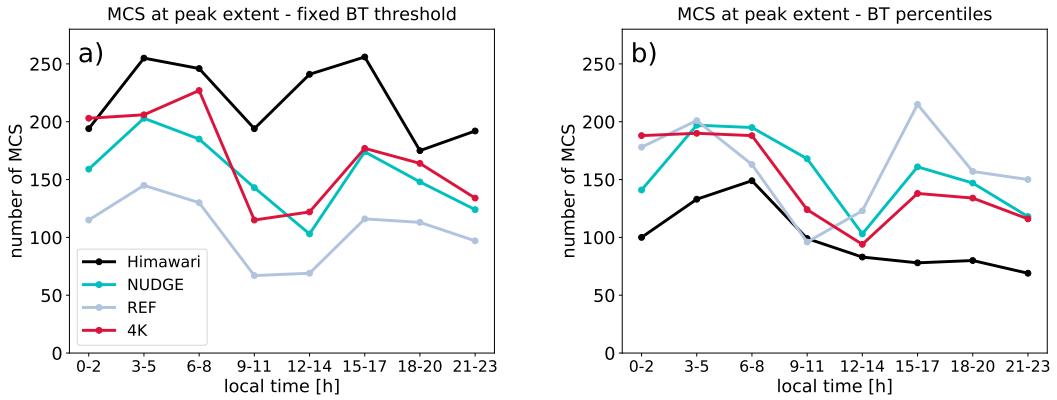

Figure 5. Diurnal cycle of peak MCS extent for (a) the fixed BT threshold and (b) the percentile based BT threshold.

In summary, the model can reproduce the simulated cold cloud fraction despite some biases in the simulation of MCS evolution, which originate from the underestimation of the coldest BT. The performance of the model in simulating large tropical MCS is satisfactory, given the use of convective parameterization and a resolution of 0.25°x0.25°, which is barely able to dynamically resolve MCS. For a more extended evaluation of E3SM using traditional evaluation metrics, the reader is referred to Xie et al. (2018); Y. Zhang et al. (2019); Rasch et al. (2019); Caldwell et al. (2019).

3.2 A Lagrangian perspective on anvil cloud evolution

Figure 6 displays the cloud fraction in the vertical column at the trajectory location following detrainment for trajectories calculated (a) neglecting (NOSEDI) or (b) including (SEDI) ice crystal sedimentation. The trajectory launching points occur at different altitudes, ranging from 10 to 13 km, with a median elevation of about 11 km. The trajectories start in regions of active convection with resolved vertical winds that are strong enough to loft the detrained air parcels and ice for about 2 km (NO SEDI) or 1 km (SEDI) within the first 5-8 hours after the trajectory is initialized. After the initial ascent the NOSEDI trajectories stay at approximately constant altitude of 11-15 km, and follow the altitude of the decaying peak in anvil cloud fraction (Fig. 6a) but stay above the peak of cloud ice (Fig. 6b). On the other hand, SEDI trajectories descend together with the mean IWC after about 6 hours, when ice crystal sedimentation dominates over the weakening large-scale ascent (Fig. 6d). SEDI trajectories also show a large spread in altitudes, extending between 7.5 and 14 km at their 5 and 95 percentile values 15 hours after initialization. This points at a large spread in simulated ice crystal radii. Moreover, SEDI trajectories travel below the peak in anvil cloud fraction, indicating a possible role of new ice crystal nucleation in maintaining the simulated anvil cloud at the later stage of its development (Fig. 6c). The convective scheme is not only detraining condensed water but also vapor, which enhances the humidity in the detrained layers during at least 40 h after the initial convective event. The relative humidity with respect to ice on average exceeds 100% in areas of active detrainment, and is maintained at values beyond 70% in the MCS outflow in the tropical tropopause layer between 14 and 17 km altitude (not shown). The increased relative humidity in the convective outflow layer offers an alternative explanation for an anvil cloud maximum above the SEDI trajectories, given the dependence of the cloud fraction scheme to the total humidity that includes specific humidity contributions from both vapor and ice condensate (Gettelman et al., 2010).

Figure 7 shows the gradually decreasing fraction of cloud-containing trajectories, reaching 50% about 15 hours after detrainment for the SEDI case. We separate the anvil evolution in three stages: thick (IWC $>$ 30 mg kg^{-1}), intermediate (30 mg kg^{-1} $>$ IWC $>$ 3 mg kg^{-1}), and thin (IWC$<$ 3 mg kg^{-1}).Thick anvils quickly decay within the first 5 hours, intermediately thick anvils dominate the cloud distribution between hour 5-10, and thin anvil clouds are dominant about 11 hours after the trajectories are initialized. A lifetime sensitivity study using different assumptions for the trajectory selection, trajectory computation, and minimum IWC and cloud fraction limits, can be found in the supplement in Fig. S1 and the associated Text S1.

3.2.1 Lagrangian anvil cloud ice mass balance

We present the dominant sources and sinks of ice during the evolution of the anvil cloud from its thick (hour 0-4) to thin stage (hour 10 and beyond) using SEDI trajectories. The trajectories start at locations with IWC median values of about 60 mg kg^{-1}, decreasing to below 10 mg kg^{-1} over the course of the first 10 hours of the cloud evolution (Fig. 9). The median in-cloud ice crystal number decreases with evolution from about 4000 g^{-1} (or about 800 L^{-1} at the detrainment level) to 1000 g^{-1}. The ice crystals initially grow slightly from 35 to 40 μm, with a slowly decreasing radius in the later stages of the development.

The net water vapor deposition (which includes both growth by deposition and shrinking by sublimation) is the dominant source of ice over the whole anvil cloud lifetime (Fig. 8). The net deposition is particularly large initially as most of the trajectories are supersaturated with respect to ice, supporting ice crystal growth (not shown). The direct detrainment of ice mass (with an assumed effective ice radius of 12 μm) from the convective cores represented by the G. J. Zhang and McFarlane (1995) parameterization is an important source of ice in the first 2 hours of the anvil evolution, indicating the presence of active deep convection. Despite focusing on trajectories at temperatures colder or near the homogeneous freezing temperature of water, the growth of ice crystals at the

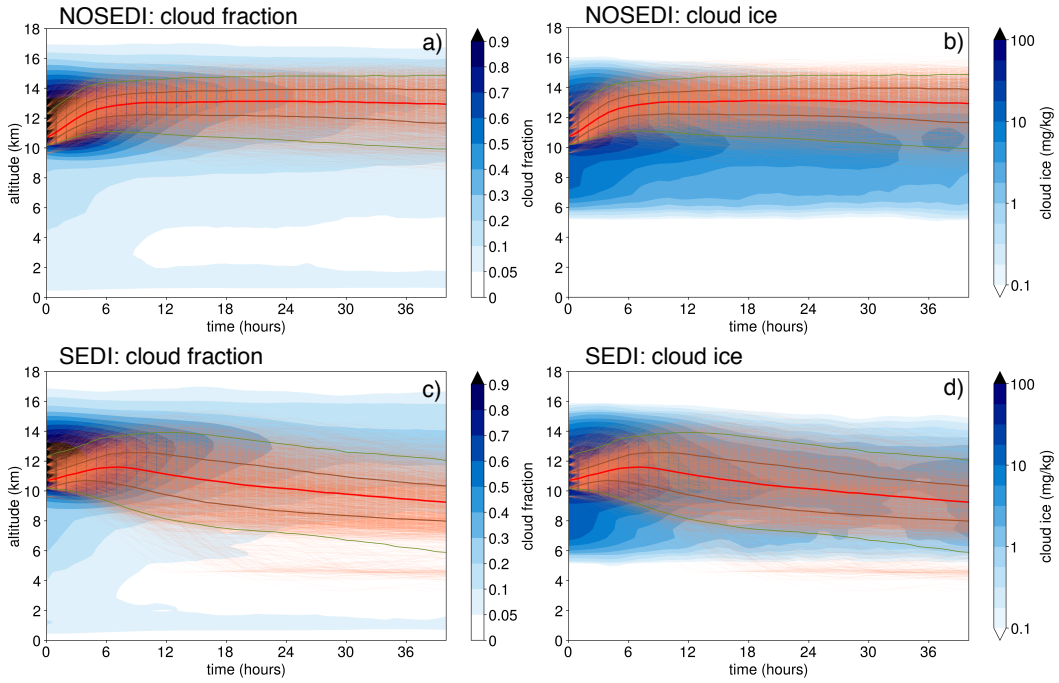

Figure 6. Altitude of a random sample of 5000 trajectories (in orange) for (a,b) NOSEDI and (c,d) SEDI as a function of time after the launch of trajectories. Plotted in the background is the mean cloud fraction in columns containing trajectories (a,c) and the gridbox mean cloud ice (b,d). The red line represents the median trajectory altitude, the brown lines the 25th and 75th percentile values, the green lines 5th and 95th percentile values.

expense of water droplets (Bergeron-Findeisen process) cannot be fully neglected in the first 6 hours of the evolution as some of the trajectories experience temperatures warmer than -35°C where part of the detrained condensate is in liquid form. Finally, the contribution of new ice crystal nucleation to the ice mass tendency is generally negligible. On the other hand, snow formation via ice crystal aggregation is the dominant sink of ice throughout the full lifecycle of anvil clouds. Aggregation moves ice crystals that cross the temperature dependent threshold size to snow and therefore increases with the growth of ice crystals. Accretion is the removal of ice crystals by collisions with snowflakes and is an important sink of ice in the precipitating stage of the anvil cloud, i.e. in the first 3-5 hours of the anvil evolution. Interestingly, ice crystal sedimentation is only of secondary importance compared to aggregation even in the thin anvil stage, beyond hour 10 of the trajectories. We note, however, that the tracked sedimentation tendency is computed from an Eulerian perspective. In the Lagrangian ice-crystal-following perspective, the trajectories are moving together with the sedimenting ice mass, therefore effectively setting the sedimentation tendency to zero in a Lagrangian sense.

3.2.2 Radiative evolution

Anvil ice microphysical properties are tightly related to the radiative effects and climatic effects of anvil clouds. Freshly detrained thick anvil clouds that contain large IWC are very reflective to visible radiation and have therefore a large shortwave cloud radiative effect (SWCRE). They also effectively prevent LW radiation from escaping to space from lower lying, warmer layers of the atmosphere, resulting in a large LWCRE. Interestingly, the averaged radiative effects along the trajectories start with a positive

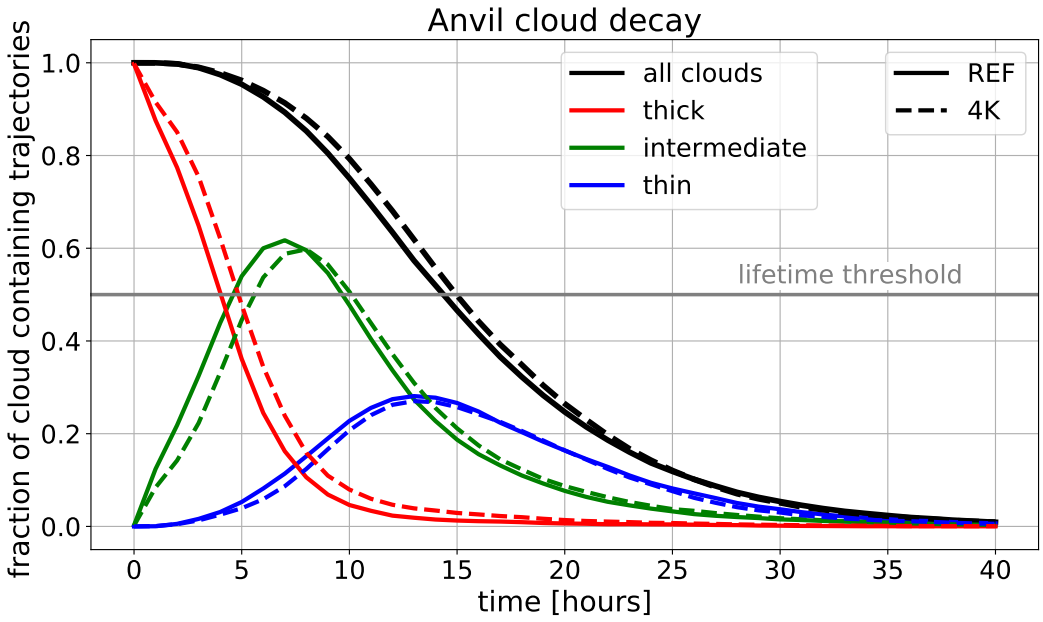

Figure 7. Fraction of trajectories that are containing a cloud for REF and 4K simulations (in black), divided into thin, intermediate, and thick categories (in red, green, and blue, respectively). The sum of the three cloud categories is equal to the "all clouds" line.

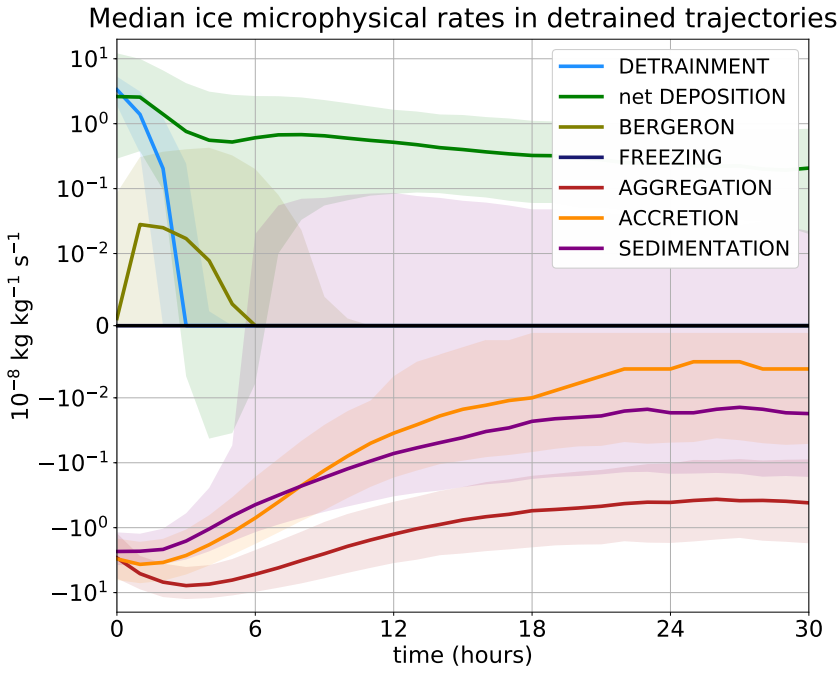

Figure 8. Lagrangian mass budget along trajectories containing ice cloud during the first 30 hours of evolution from the REF simulation. The shaded area represents the spread between the 25th and 75th percentile values.

net CRE, which gradually decreases in the first 4-5 hours of the anvil evolution (Fig. 10a),

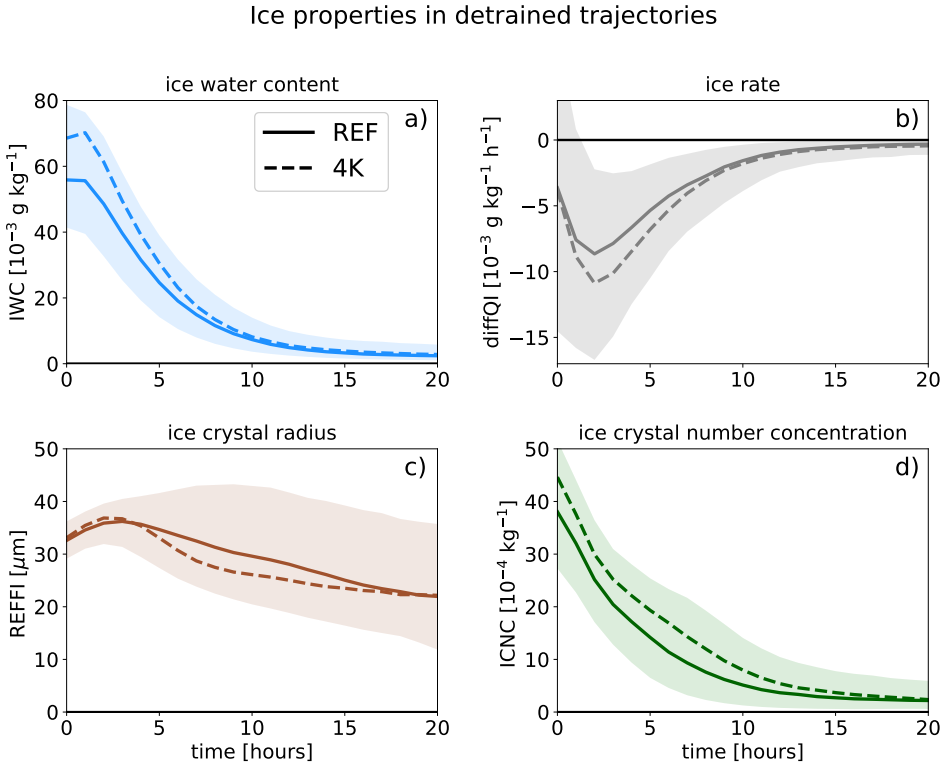

Figure 9. Median in-cloud ice water content (IWC), in-cloud ice crystal number concentration (ICNC), in-cloud ice crystal radius (REFFI), and ice rate (diffQI) in detrained trajectories. diffQI is defined as the sum of all ice sources and sinks of ice plotted separately in Fig. 8. Shaded area represents the spread between the 25th and 75th percentile values for REF.

despite decreasing IWC, ice crystal number, and consequently cloud albedo. This can be explained by the average insolation that the tracked clouds receive over the course of their lifetime (Fig. 10b). The mean insolation starts at values of about 280 W m^{-2} and almost doubles within the first 10 hours. The peak in MCS activity, where trajectories start, occurs during early morning hours just before sunrise, on average (Fig. 5b). Within a few hours, most of the trajectories are exposed to higher insolation values near mid day, leading therefore to a larger SWCRE causing the net CRE to shift to negative values (Fig. 10a,b). At this point both SWCRE and LWCRE start decaying significantly. The averaged CRE along trajectories for 15 hours of cloud evolution exceed values of 100 W m^{-2} in terms of LWCRE and SWCRE, with a small negative net CRE term (Tab. 3). These results are not very sensitive to the trajectory selection criterion, as shown by computing radiative fluxes along all computed trajectories (Tab. S1).

4 Results - future climate

4.1 Mean climate responses to warming

We first evaluate mean climate responses to warming for the Tropical Western Pacific. The model simulates a 40% increase in precipitable water and a 20% increase in liquid water path for the clim4K simulation (not shown) with very little change in relative humidity (Fig. 11f).

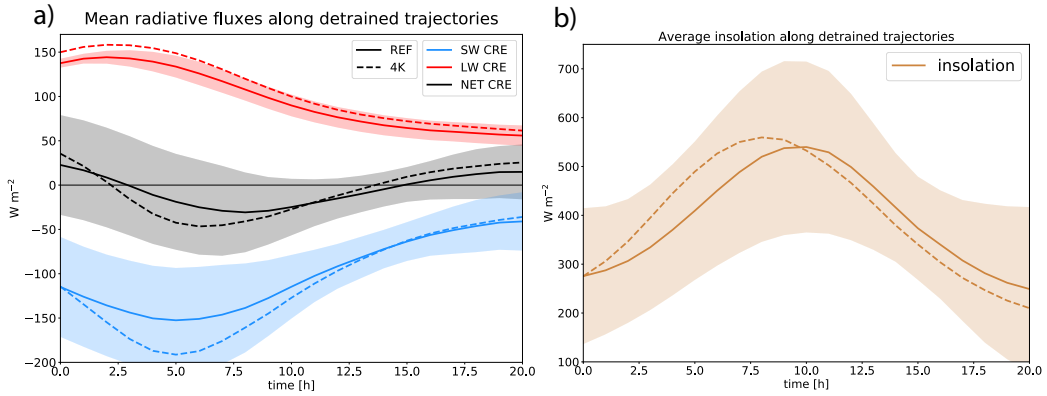

Figure 10. (a) CRE along detrained trajectories for the two simulations. Shaded area represent one standard deviation for REF. (b) Mean insolation values along tracked trajectories for the two simulations. Shaded area represent one standard deviation for REF.

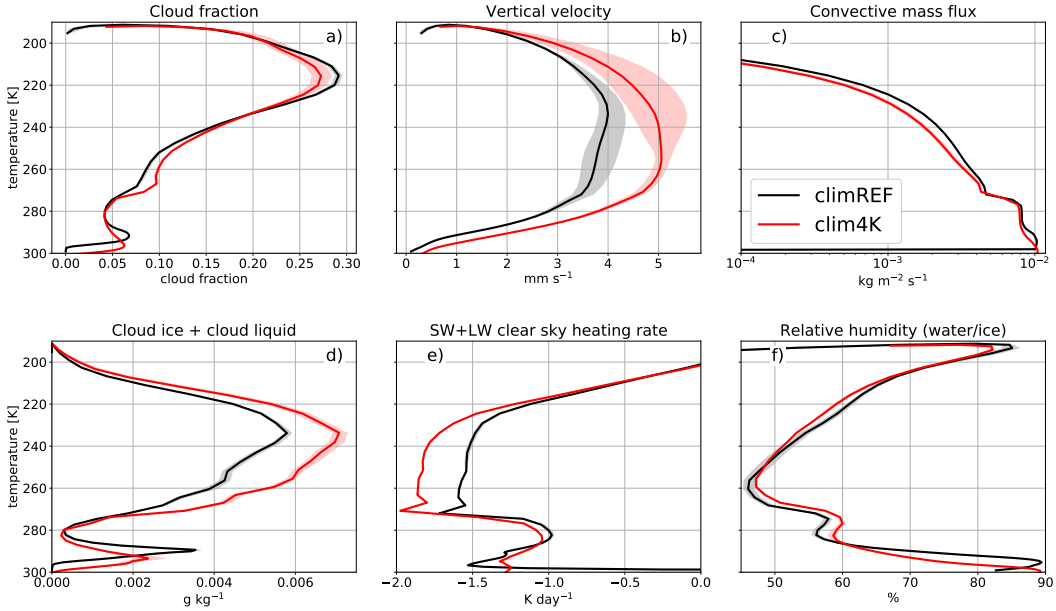

Figure 11. Domain averaged cloud fraction (a), vertical velocity (b), convective mass flux from the convective parameterization (c), cloud ice and liquid (d), clear sky heating rates (e), and the relative humidity with respect to water (for T>273 K), ice (for T<253 K), or a mixture between the two (for 273>T>253 K). The quantities are plotted in function of temperature between the surface and approximately the tropopause level. Shaded areas cover the space between all 3 annually averaged values for each of the simulations.

IWC increases significantly with global warming (Fig. 11d) at all temperatures, particularly in the 230 to 250 K range (Fig. 11d). This is consistent with increases in clear-sky cooling rates (Hartmann et al., 2020). The peak in anvil cloud amount remains at temperatures between 220 and 212 K in both simulations (Fig 11a). The anvil cloud fraction decreases with warming, which is consistent with a decrease in the upward mass flux by the convective scheme (Fig. 11c). In contrast to the convective mass flux, the resolved mean vertical velocity increases in the global warming simulation (Fig. 11b).

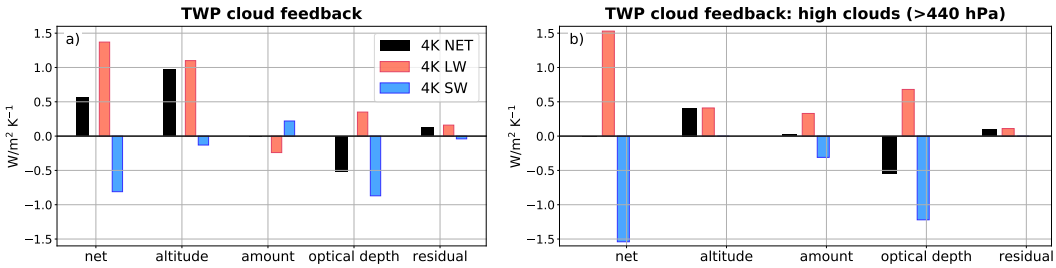

Figure 12. (a) Total net cloud feedback decomposition for the Tropical Western Pacific (TWP). (b) Same but for high clouds only, showing also the LW (red) and SW (blue) cloud feedback components.

The domain-mean in-cloud COD that considers changes to cloud reflectivity only without taking into account changes in cloud fraction, increases by 3.8% in the clim4K simulation. The changes in ice clouds lead to a small and negative net CRE change of about 2 W m^{-2}. The cloud feedback decomposition using Zelinka et al. (2016) method shows a strong positive feedback attributed to the increase in cloud altitude (Fig. 12a). However, the aforementioned increases in COD lead to a negative feedback that counteracts about half of the altitude feedback.

Figure 12b shows the decomposition of cloud feedback for high clouds (<440 hPa) only. The net feedback is near zero, despite large SW and LW components. In the case of high clouds, the positive altitude feedback is fully counteracted by the negative optical depth feedback. The cloud amount feedback has significant SW and LW components that are nearly equal in size. The increased COD does not lead only to a strong SW feedback, but also to a significant positive LW feedback. This is expected due to near neutral net CRE of anvil clouds where an increase in COD would also lead to a significant increase in LWCRE (Berry and Mace (2014); Hartmann and Berry (2017) and also Fig. 10).

4.2 MCS responses

The cold cloud area representing very thick and moderately thick high clouds increases from 8.5% (REF) to 9.4% (4K) which is expected from the increase in vertical velocity and domain average cloud ice (Fig. 11b,d). If MCS are tracked by using fixed BT thresholds of 210 and 240 K, the number of MCS increases by 60% in the 4K simulation in spite of no change in their lifetime (Tab. 2). The simulated increase in MCS number is consistent with studies of MCS responses to global warming over the continental United States (Prein et al., 2017; Diffenbaugh & Giorgi, 2012). On the other hand, a percentile-based MCS selection criteria approach does not indicate a much higher MCS number in the 4K simulation. The maximum MCS extent and lifetime remain approximately the same between REF and 4K simulations with both MCS selection methods. The tracked MCS show increases in precipitation, which is expected given the increase in precipitable water under global warming (not shown). Moreover, a warmer climate increases the saturation deficit of the tropical atmosphere, leading to a larger buoyancy of deep convection and consequently an increase in convective available potential energy (CAPE) (Seeley & Romps, 2015). The BT-based detection limits do not allow for a good estimate of changes to the evolution and thinning of anvil clouds. In order to study such changes we return to an analysis along trajectories.

4.3 Cloud and radiative responses to warming along detrained trajectories

4.3.1 Responses of anvil cloud lifetime and cloud properties

The IWC increases with warming along the trajectories, particularly in the initial thick anvil stage (Fig. 9a). The ice crystal number concentration also increases, while the ice crystal radius remains initially roughly unchanged and decreases slightly with respect to REF only in the late stage of the anvil evolution (Fig. 9c). The lifetime of the anvil cloud remains roughly constant (Fig. 7). However, the larger initial IWC leads to a 1 hour increase in the lifetime of the thick part of the anvil cloud, or a 20% relative increase in the thick anvil cloud lifetime. The result does not change if we include in the analysis also trajectories influenced by new occurrence of convection in later stages of their evolution (Fig. S2).

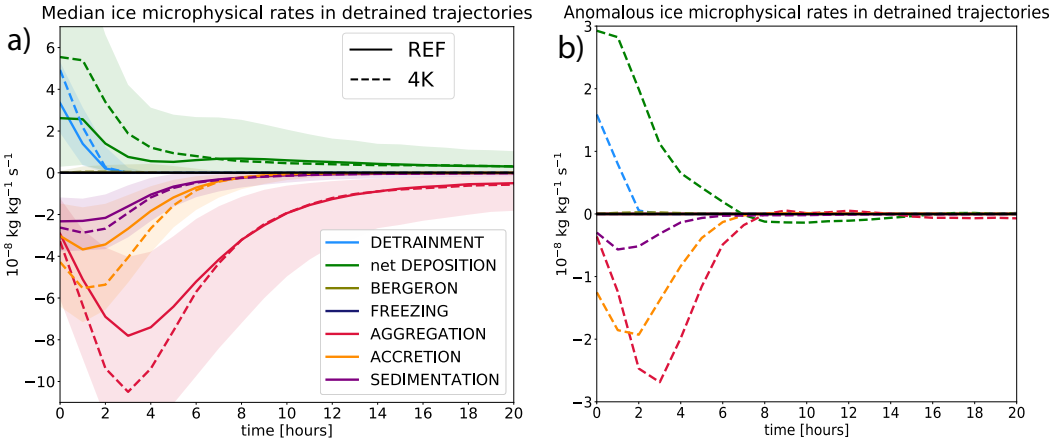

Figure 13. (a) Median sources and sinks of ice in the 3 simulations. Shaded area represents the spread between the 25th and 75th percentile values for REF. (b) Anomalies of median values of source and sinks of ice with respect to REF.

The microphysical process rate evolution shows a different behavior between the early and late stage of anvil evolution (Fig. 13):

- in the early stage of anvil evolution (hour 0-6) both sources and sinks of ice increase in amplitude with respect to REF
- in the late stage of anvil evolution (hour 7-20) sources and sinks of ice are similar with respect to REF.

The trajectories indicate that the 4K simulation starts at a larger IWC due to both a 40% increase in detrainment of ice as well as a 80-100% increase in the net deposition flux (Fig. 9). Specific humidity near the deep convective detrainment level increases as the anvil cloud peak shifts to higher altitudes at lower air densities, while remaining at the roughly constant temperature (not shown). This decrease of the average detrainment level pressure from about 235 to about 200 hPa leads to a 5-10% increase in the deposition flux based on a temperature and pressure dependent depositional growth equation (Lohmann et al., 2016), which explains part of the deposition tendency increase. Moreover, a larger static stability near detrainment level in a warmer world may decrease the mixing of detrained air parcels with environmental air, therefore additionally increasing the IWC in the early stage of anvil cloud development.

Table 3. Mean changes in cloud radiative effects (CRE) during the 20 h long trajectories. The SWCRE is in the last column calculated using average insolation value of 390 W m^{-2}

.

	REF	**4K-REF**	**4K-REF ConstInsol**
LW CRE [W m^{-2}]	99.0	10.7	10.7
SW CRE [W m^{-2}]	-105.4	-12.8	-10.2
NET CRE [W m^{-2}]	-6.4	-2.1	0.6
NET feedback [W m^{-2} K^{-1}]	/	0.5	1.1

On the other hand, in the 4K simulation the rate of loss of atmospheric ice increases proportionally with the increase in IWC to first order, which results in only a small increase in thick anvil cloud lifetime (Fig. 7). Ice crystal aggregation transfers the larger crystals to snow when they cross a temperature dependent ice crystal radius threshold, which spans between 100 - 125 μm for the relevant range of temperatures. Since the trajectories invariably originate near convective events, the initial ice crystal radii are close to the prescribed ice crystal radius detrained from the convective parameterization which is set to a constant value of 12 μm, leaving little opportunity for early changes by aggregation between the control and warming runs. The aggregation rate increases by about 20-30% between hours 1-5 of the anvil development, probably due to a general increase in IWC. This is also the likely cause of an increase in both accretion and sedimentation tendencies. In the late stage of anvil evolution the net deposition slightly decreases compared to REF. This may be connected with a 12% decrease in ice crystal radius (Fig. 9) leading to a 23% decrease in surface area available for deposition, given no simulated change in relative humidity and comparable IWC between REF and the warming simulation (Fig. 11f).

4.3.2 Radiative responses and climatic implications

The increase in IWC and ice crystal number with warming leads to a larger SWCRE as shown in Fig. 10a. At the same time clouds become more opaque for OLR, resulting in an increased LWCRE. The average net CRE for the whole lifecycle of tracked anvil clouds is slightly more negative (Tab. 3), partially due to increases in COD, consistent with the domain average increases in in-cloud COD (see Section 4.1). In addition, net CRE is more negative also due to an increase in mean anvil cloud insolation during the first 8 hours of cloud development. This is caused by a small shift in the diurnal cycle of MCS (Fig. 10b) responsible for a 50 W m^{-2} insolation increase between hour 2 and 7 in the 4K simulation. The insolation-driven changes in SWCRE are partially compensated by the insolation anomalies of the opposite sign at the late stage of the anvil cloud development (after hour 10). However, at that point in the lifecycle, the anvil clouds are not as reflective as in their initial stage, leading only to a minor modulation of the incoming SW radiative flux. In summary, the increases in SWCRE dominate over increases in LWCRE and lead to a more negative net CRE balance over the course of the anvil cloud lifecycle (Tab. 3 and Fig. 10a). This negative CRE anomaly is consistent with the domain averaged negative high cloud optical depth feedback (Fig. 12).

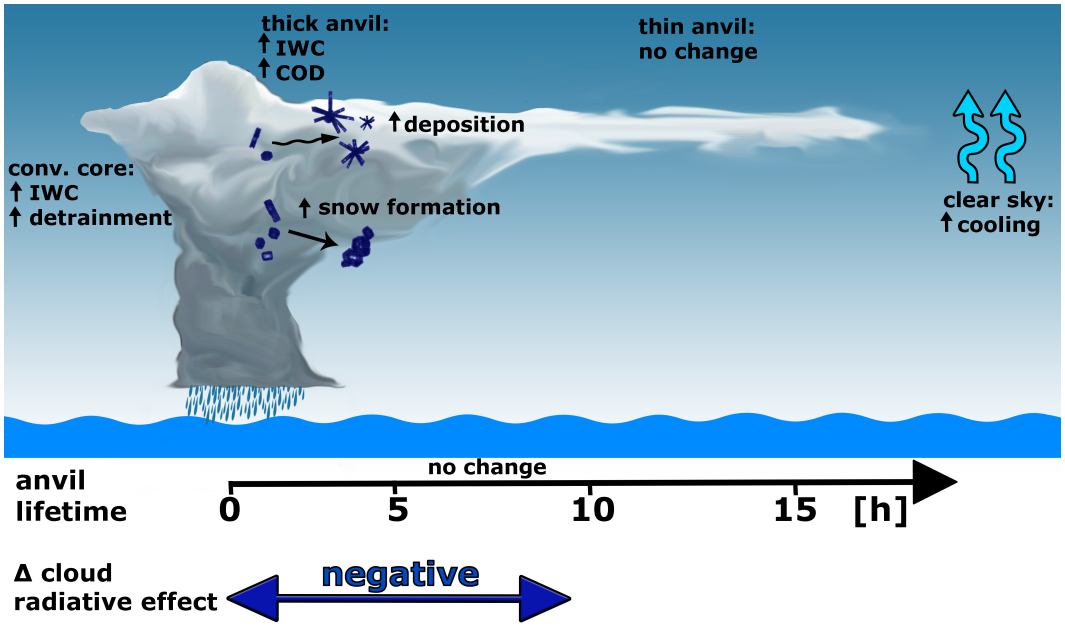

Figure 14. Summary sketch highlighting major changes with global warming. The increase in cloud altitude is omitted from the sketch.

5 Discussion

5.1 Implications for tropical high cloud feedbacks

Figure 14 summarizes the main findings of the previous section. The IWC in thick anvils increases due to increased detrainment tendency from deep convective cores and increased deposition flux. This leads to an increased COD and a negative net CRE anomaly in the early stage of the anvil lifecycle. The changes are smaller in aged thin anvil clouds, as the sinks of ice, particularly snow formation, becomes more efficient in removing the excess IWC. At this point we take a step further to transform the net CRE values of Table 3 into climate feedbacks by dividing the change in net CRE along trajectories by the increase in globally averaged surface temperatures and adding a derived cloud masking correction term, as explained in Appendix A. The computed climate feedback along detrained trajectories is small and positive for the 4K simulation and consistent with the results of the 3 year long clim4K simulation (Fig. 12a) as well as with the literature finding a robust positive tropical cloud feedback (Zelinka & Hartmann, 2010; Zelinka et al., 2012b, 2013; Boucher et al., 2013) with the dominant cloud altitude LW feedback component due to a 1-1.5 km increase in high cloud altitude.

Our simulations reveal in addition an increase in precipitable water and large-scale updraft velocities with global warming that lead to increasing condensed water content at temperatures below freezing, despite a counteracting decrease in the convective mass flux. The anvil cloud peak stays at approximately the same temperature level consistent with the FAT theory (Hartmann & Larson, 2002). When clouds shift in altitude, they shift to an environment with higher static stability, which according to Bony et al. (2016) implies a decreased convective detrainment and a decrease in anvil cloud fraction. In our simulations anvil cloud fraction decreases, but domain-averaged cloud ice content increases, leading to a larger optical depth of remaining anvil clouds and a negative optical depth feedback.

Part of the reason for the increase in cloud ice is that the dynamic environment in a warmer climate is more favorable for deep convective development as shown by increased large-scale vertical velocity profiles (Fig. 11b) likely caused by the narrowing of the Intertropical Convergence Zone (Byrne & Schneider, 2016; Byrne et al., 2018). On the other hand, the upper tropospheric radiative cooling rates increase with warming (Fig. 11e). As the climate in our region of interest can to a large degree be approximated by the radiative convective equilibrium, the additional radiative cooling must be compensated by increases in latent heating (Jakob et al., 2019; Hartmann et al., 2020). The increase in cloud ice provides this additional heat.

We also observed increases in cloud reflective properties and ice removal rates with warming (Figs. 10 and 13) due to an increase in anvil cloud precipitation efficiency by ice crystal aggregation and accretion of ice crystals by snow. However, most of this increase in precipitation (snow) formation is due to a higher IWC at the starting points of anvil trajectories near the main detrainment level. Moreover, it is not only the sinks but also the sources of ice that increase, in particular the net deposition flux, leading to little change in anvil cloud lifetime nor any substantial shifts of the proportion of thick vs. thin anvil clouds (Fig. 7). The simulated changes in anvil clouds are therefore different from the microphysical Iris hypotesis and its negative anvil cloud feedback proposed by Lindzen et al. (2001).

5.2 Potential changes of anvil cloud diurnal cycle and the associated radiative impacts

The average local time of peak surface area of tracked MCS shifts from about midnight in REF simulation to 4 am in the 4K simulation (Fig. 5), because more MCS peak in the morning hours. This increases the SWCRE and leads to an additional negative (diurnal) cloud feedback component that cannot be evaluated with the cloud feedback decomposition method used here, because the ISCCP simulator, which it is based on, is active only in sunlit gridboxes, and represents daytime average cloud fraction computed from 3-hourly instantaneous snapshots, meaning that it is not suitable for studying variations in the diurnal cycle of clouds. We additionally compute CRE by assuming diurnally averaged insolation of 390 W m^{-2}, representative of the domain mean insolation during the months June-August in the tracking region, which increases the net CRE budget by 2.7 W m^{-2}, implying a 0.6 W m^{-2} K^{-1} larger net cloud feedback (Tab. 3). In other words, the more negative SWCRE balance when using model calculated insolation instead of its diurnal average leads to a negative diurnal cycle component of cloud feedback of 0.6 W m^{-2} K^{-1}.

A possible explanation for the delayed morning MCS peak may be the increase of the saturation pressure deficit (difference between specific humidity and saturation specific humidity) with warming. The saturation deficit was shown to play an important role in delaying the onset of deep convection both over land and ocean (Chaboureau et al., 2004; Khairoutdinov & Randall, 2006; Kuang & Bretherton, 2006). The same mechanism was shown to be responsible for an increase in CAPE with global warming (Seeley & Romps, 2015). A larger mean saturation deficit could lead to a longer "precondition" time of the free troposphere, delaying the onset of deep convection.

5.3 Verification of cloud radiative effect changes with global warming along detrained trajectories

We provide an alternative and simplified view of the anvil lifecycle by binning the model output based on ice water path (Fig 15d-f) to verify CRE anomalies calculated along anvil cloud trajectories. The highest IWP percentile values represent grid boxes of active deep convection and fresh anvil clouds that gradually evolve into non-precipitating anvils somewhere near the crossover point between net negative and positive CRE, at about the 80th percentile of ice water path based on observational data (Kubar et al.,

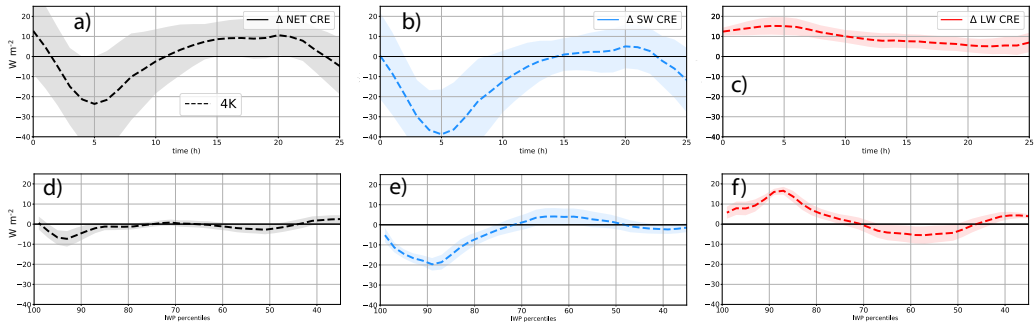

Figure 15. CRE anomalies of 4K simulation with respect to REF along detrained trajectories (a-c) and in a ice water path binned perspective (d-f). The shading represents half a standard deviation of each data point.

2007; Gasparini et al., 2019). This part of the anvil lifecycle corresponds to the first 6-10 hours of the evolution along trajectories. The radiative flux anomalies computed with the help of trajectories and IWP binning show a consistent behavior: a more negative net CRE balance compared to REF, which is the strongest after hour 3-7 from the beginning of the trajectory or at 94-92 IWP percentile value (Fig. 15a,d). This shift is dominated by the increase in SWCRE and is partially counteracted by the increase in LWCRE (Fig. 15b,c,e,f). The further evolution shows a small positive net CRE anomaly in the late stage of cirrus evolution after about 10 hours of trajectory tracking, which is not observed in the IWP binned perspective, where the net CRE anomaly remains near zero in the 75 to 55 percentile range (Fig. 15d). The ice water path binning perspective nevertheless agrees to a large extent with the CRE anomalies along the cloud-containing trajectories. Note however, that only the trajectory approach offers a direct estimation of anvil properties along the cloud decay without additional assumptions and reveal the lifetime aspect, which cannot be estimated by the IWP binning approach.

5.4 Study limitations

The goal of this study is to provide a better understanding of the anvil cloud evolution in present and future warmer climate by using an intuitive, ice crystal following Lagrangian perspective. Models are currently the only possible way to provide such insights into cloud lifecycles due to limitations in in-situ and satellite observational data. While the method applied indeed provides valuable insights into the behavior of the model, the reader should be aware of its possible limitations as outlined below.

5.4.1 Statistical robustness

The core part of the study (MCS tracking and trajectory analysis) relies on a 3 month simulation following a 7 day spin up period. 92 simulated days are enough to represent part of the tropical intraseasonal variability at the synoptic timescale with disturbances of sizes of about 1000 km and timescales of 1-10 days encompassing typical convectively coupled equatorial waves (Kiladis et al., 2009). The length of the simulation is not long enough to encompass a whole possible cycle of the Madden-Julian oscillation with a typical period of 30-70 days. However, while this may influence the number of tracked MCS, it is not expected to have a large impact on the anvil cloud lifecycle itself. The anvil decay is primarily driven by processes that operate on a fast timescale like microphysics and radiation, and we have sampled many occurances of the anvil decay process. Interannual variability, e.g. ENSO, could be an issue, but the simulations use prescribed SST,

which prevents the model drift into a different ENSO phase allowing for a better comparison between the simulations. Nevertheless, the simulations used for computing mean climatic values in the region of interest in Section 4.1 are run for only 3 years, which is not enough for computing reliable climatologies. The short simulations therefore introduce uncertainties in CRE and cloud feedback calculations, and suggest an interannual variability in mean June-August net CRE of about 0.5 W m^{-2} in the tracking region, computed from the 3 years of available model output, which is smaller than the magnitude of the net CRE anomalies listed in Table 3. The qualitative features of the analysis are therefore probably quite robust, while the uncertainly in the quantitative amplitude may be considerable.

5.4.2 Trajectory calculation

We use an offline method for calculating trajectories from model resolved large-scale motions. The E3SM model time step is set to 15 minutes while the output time step is archived at 1 hour intervals because of storage space limitations. E3SM therefore evolves on timescales that are shorter than resolved from the archived data (4 updates of velocity and microphysical fields are performed online within the archival time interval), which introduces minor biases in trajectory calculations. We verify the magnitude of such errors by reconstructing the ice mass evolution from the sum of all ice source and sink processes. This reconstruction reproduces the simulated IWC in an excellent way, with a deviation from the model computed IWC never exceeding 2% (not shown). A study by Miltenberger et al. (2013) based on a regional weather prediction model shows only minor horizontal and vertical biases in the offline trajectory calculation when comparing offline calculated trajectories using 1-hourly model output with the online calculated trajectories for the model resolution of 14 km with the model timestep of 40 s.

5.4.3 Simulated interaction of convective and large-scale cloud processes

A large part of the presented results strongly dependends on the way E3SM simulates deep convection with the help of a modified version of the G. J. Zhang and McFarlane (1995) convective scheme, described in Xie et al. (2018). The scheme is meant to reduce CAPE over the course of a timescale that can be tuned. The model was found to underestimate BT of the strongest convective events, and at the same time overestimate the frequency of intermediate BT. This biases indicate a too shallow convective cloud top layer and/or a too small convective mass flux above about 10 km altitude which is consistent with findings by Y. Zhang et al. (2019) and Xie et al. (2018). This may be caused by a too large convective entrainment (Wang & Zhang, 2018) and/or a low mid tropospheric humidity bias (Xie et al., 2018). Moreover, convection is typically found to be shallower in models with higher vertical resolution (like E3SM) compared to those with coarser resolution (e.g. CESM) as a higher vertical resolution can lead to stronger vertical gradients in humidity, heating, and static stability (Rasch et al., 2019).

The deep convective scheme uses a simple thermodynamical treatment of clouds, with a temperature dependent partitioning of detrained condensate between liquid and ice. Besides condensate it also detrains vapor, leading to a moistening of the upper troposphere. The convective microphysics is very simplified and only 1-moment in contrast to the 2-moment stratiform cloud microphysical scheme. The convective part of the code therefore does not explicitly calculate ice crystal radii, while the 2-moment stratiform cloud microphysics requires a mass and size or number of detrained ice particles. The convective scheme provides this information in an arbitrary way - the detrained ice crystal radius is a tunable parameter, set to 12 μm in the model version used here. This is inconsistent with observational evidence, which shows that the ice particle size in convective cores decreases with altitude (Van Diedenhoven et al., 2016; van Diedenhoven et al., 2020) and may therefore lead to an underestimation of the lifetime of the detrained ice crystals at the convective cloud tops and overestimation at lower levels. Neverthe-

less, despite the use of parametrized convection and its associated problems, we found E3SM to reproduce the observed albedo-OLR histogram in the tracking region remarkably well and to simulate MCS in a reliable way compared to geostationary observations of tropical maritime convection.

6 Conclusions

Tropical net CRE is determined by anvil clouds at various stages of evolution. In this study we first used a cold cloud tracking algorithm to follow the evolution of MCS in the Tropical Western Pacific. The MCS simulated by E3SM were compared with the observed MCS from 3 months of Himawari geostationary satellite data. The comparison showed that the model is, despite some deficiencies, able to reproduce many features of the observed albedo-OLR pairings representing anvil cloud decay as, well as MCS and their diurnal cycle. We find that cloud ice amount increases on a warmer Earth, which leads to a negative cloud optical depth feedback. However, the net cloud feedback is positive due to the dominant positive cloud altitude feedback.

In a second analysis step, we diagnosed anvil properties following trajectories launched from gridboxes with active convection at the peak of the MCS lifecycle in the E3SM simulations. These trajectories follow the detrained ice crystals throughout the evolution of the anvil clouds, from their inital thick to final thin stage. We use the trajectories to estimate the anvil cloud lifetime, which was found to be about 15 hours. The anvil properties and their CRE initially evolve very quickly, with the thick anvil stage lasting only about 2-5 hours, despite a supporting dynamical forcing in the form of the strong updraft velocity. The updraft on average exceeds the sedimentation velocity of tracked ice crystals in the first 6 hours of cloud evolution. The anvil gradually continues to decay with decreasing IWC and ice crystal number concentration, resulting in decreases of both SWCRE and LWCRE. The dominant source of ice is ice crystal growth by deposition, while the dominant sinks are snow formation by ice crystal aggregation (ice is converted to snow when crossing the aggregation cutoff size) and accretion (ice is removed when scavenged by falling snow). Sedimentation of ice crystals plays only a secondary role.

We evaluated changing anvil cloud properties using present day SSTs, and SSTs incremented by a uniform 4K increase to identify changes that might occur in anvils with global warming. Figure 14 represents a summary of the main simulated changes in clouds. In general, we observe an increase in in-cloud COD for thick high clouds due to an increase in detrained IWC and vapor. Ice mass sources and sinks increase, leaving the anvil cloud lifetime roughly unchanged. Changes to anvil microphysics lead to more negative SWCRE in the thick and intermediately thick anvil cloud stage in the first 10 hours of anvil cloud evolution. The changes in the thin anvil stage are small, which leads to a net negative CRE response along the full anvil lifecycle.

The estimation of cloud feedbacks along trajectories indicated a feedback of about 0.5 W m^{-2} K^{-1}. This result is consistent with the mean climate feedback computed with the help of radiative kernels in which the positive altitude feedback dominates over a smaller contribution due to the COD increase. The feedback may also have a negative component due to a shift in peak deep convective activity occuring at a later time in the morning, leading to more reflected SW radiation.

Our study shows how a Lagrangian, ice-crystal following approach can provide an in-depth and more intuitive perspective on anvil cloud evolution and its changes with global warming. Our approach is complementary to the standard global or regionally averaged climate feedback decompositions. In particular, it offers the following advantages over the standard mean-climate perspective:

- It gives a direct estimation of cloud lifetimes

- It offers an intuitive perspective on microphysical processes that control anvil evolution and radiative properties. It also allows computing Lagrangian mass budgets
- It provides a straightforward and unbiased way of separating cloud responses based on cloud development stage

Such Lagrangian approaches are needed if we want to fully understand the mechanisms of the anvil cloud lifecycle and how they respond to global warming. A Lagrangian, air parcel or hydrometer following approach can provide new insights into the evolution of cloud and other climate processes. The use of Lagrangian methods in high resolution models is still limited and should be made a priority, particularly by the implementation of online trajectory modules (Miltenberger et al., 2013). Follow-up studies using Lagrangian methods could consider extending their simulations from months to years to better control noise due to natural variability. An increased statistical significance of the tracked features would for example open up new opportunities for studying potential radiative feedbacks caused by changes in the diurnal cycle of clouds, which currently cannot be captured by cloud feedback decomposition methods.

Appendix A Cloud feedback estimation from changes in net CRE along detrained trajectories

CRE are defined as a difference between all-sky and clear sky radiative fluxes. A change in CRE between the reference and a warmer climate is not equivalent to the change in cloud feedbacks, although the patterns of change generally resemble each other (e.g. Fig. 11 in Soden et al. (2008)). While cloud feedbacks refer only to the radiative effects of changes in cloud properties with warming, CRE are defined as a difference between full and clear sky radiative fluxes and therefore depends both on changes in clouds and their raditative properties as well as changes in clear sky radiation. In simulations with increased SSTs the atmospheric opacity increases mainly due to increased water vapor concentrations. This effect is stronger in clear sky regions and thus leads to a more negative CRE response compared with cloud feedbacks (Ceppi et al., 2017).

An accurate way of estimating cloud masking adjustments is to use technically challenging partial radiative perturbation methods (Colman, 2003; Soden et al., 2004) , which goes beyond the scope of our work. We therefore estimate a cloud masking correction term by using the difference between the computed CRE values for months June-August in the 3-year long simulation (row 1 in Table A1), normalized by the change in global surface temperature in the respective simulation (row 2 in Table A1), and the cloud feedback calculations with the help of radiative kernels (Zelinka et al., 2012a) (row 4 in Table A1). The derived cloud masking agrees well with the masking terms computed from offline radiative calculations with a series of GCMs (Soden et al., 2008; Zelinka et al., 2013; Yoshimori et al., 2020).

Acknowledgments
We thank Michael Sprenger for the help with the implementation of Lagranto into E3SM model. We thank Peter Blossey for numerous valuable comments that helped improve our methods and the manuscript. Thanks to Mark Zelinka for sharing the cloud radiative kernels and the cloud feedback decomposition script. This research was partially supported as part of the Energy Exascale Earth System Model (E3SM) project, funded by the U.S. Department of Energy, Office of Science, Office of Biological and Environmental Research. BG acknowledges support by the Swiss National Science Foundation projects P2EZP2_178485 and P400P2_191112 and by the National Science Foundation under Grant AGS-1549579. CJW is supported by the NOAA Climate and Global Change Postdoctoral Fellowship Program, administered by UCAR's Cooperative Programs for the Ad-

Table A1. 3 year JJA average net cloud radiative effects (CRE) anomalies with respect to reference simulation, net cloud feedback calculated by using Zelinka et al. (2012a) radiative kernels for Tropical Western Pacific. The adjustment term is computed as a difference between the cloud feedback and normalized CRE value.

	clim4K
Δ NET CRE [W m^{-2}]	-2.03
Δ temperature [K]	4.31
$\frac{\Delta NETCRE}{\Delta temperature}$ **[W m^{-2} K^{-1}]**	-0.47
calculated feedback [W m^{-2} K^{-1}]	0.52
estimated CRE adjustment [W m^{-2} K^{-1}]	0.99

vancement of Earth System Science (CPAESS) under award #NA18NWS4620043B. MD acknowledges support by the Swiss National Science Foundation project P2EZP2_178439.

Simulations were performed using computer resources provided by EMSL (grid.436923.9), a DOE Office of Science User Facility sponsored by the Office of Biological and Environmental Research and located at Pacific Northwest National Laboratory. The Himawari-8 data were obtained from the Atmospheric Science Data Center of the NASA Langley Research Center and are available at https://earthdata.nasa.gov/. The satellite data from the A-Train Integrated CALIPSO, CloudSat, CERES, and MODIS Merged Product Release B1 (CCCM) were obtained from https://search.earthdata.nasa.gov. The data and plotting scripts will be made available on Zenodo (10.5281/zenodo.3893226) after the final acceptance of the publication.

References

Avery, M., Winker, D., Heymsfield, A., Vaughan, M., Young, S., Hu, Y., & Trepte, C. (2012). Cloud ice water content retrieved from the CALIOP space-based lidar. *Geophys. Res. Lett.*, *39*(5), 2–7. doi: 10.1029/2011GL050545

Berry, E., & Mace, G. G. (2014). Cloud properties and radiative effects of the Asian summer monsoon derived from A-Train data. *J. Geophys. Res. Atmos.*, *119*, 9492–9508. doi: 10.1002/2014JD021458

Bessho, K., Date, K., Hayashi, M., Ikeda, A., Imai, T., Inoue, H., ... Yoshida, R. (2016). An introduction to Himawari-8/9 — Japan's new-generation geostationary meteorological satellites. *J. Meteorol. Soc. Japan*, *94*(2), 151–183. doi: 10.2151/jmsj.2016-009

Bodas-Salcedo, A., Webb, M. J., Bony, S., Chepfer, H., Dufresne, J. L., Klein, S. A., ... John, V. O. (2011). COSP: Satellite simulation software for model assessment. *Bull. Am. Meteorol. Soc.*, *92*(8), 1023–1043. doi: 10.1175/2011BAMS2856.1

Bony, S., Stevens, B., Coppin, D., Becker, T., Reed, K. A., Voigt, A., & Medeiros, B. (2016). Thermodynamic control of anvil cloud amount. *Proc. Natl. Acad. Sci.*, *113*(32), 8927–8932. Retrieved from `http://www.pnas.org/content/113/32/8927.abstract` doi: 10.1073/pnas.1601472113

Boucher, O., Randall, D., P. Artaxo, C. B., Feingold, G., Forster, P., Kerminen, V.-M., ... Zhang, X. (2013). *Clouds and Aerosols. In: Climate Change 2013: The Physical Science Basis. Contribution of Working Group I to the Fifth Assessment Report of the Intergovernmental Panel on Climate Change, edited by: Stocker, T. F., Qin, D., Plattner, G.-K., Tignor, M., All* (Tech. Rep.).

926 Cambridge University Press, Cambridge, United Kingdom and New York, NY,
927 USA.
928 Byrne, M. P., Pendergrass, A. G., Rapp, A. D., & Wodzicki, K. R. (2018). Re-
929 sponse of the Intertropical Convergence Zone to Climate Change: Location,
930 Width, and Strength. *Curr. Clim. Chang. Reports*, *4*(4), 355–370. doi:
931 10.1007/s40641-018-0110-5
932 Byrne, M. P., & Schneider, T. (2016). Narrowing of the ITCZ in a warming cli-
933 mate: Physical mechanisms. *Geophys. Res. Lett.*, *43*(21), 11,350–11,357. doi:
934 10.1002/2016GL070396
935 Caldwell, P. M., Mametjanov, A., Tang, Q., Van Roekel, L. P., Golaz, J. C., Lin,
936 W., ... Zhou, T. (2019). The DOE E3SM Coupled Model Version 1: De-
937 scription and Results at High Resolution. *J. Adv. Model. Earth Syst.*. doi:
938 10.1029/2019MS001870
939 Ceppi, P., Brient, F., Zelinka, M. D., & Hartmann, D. L. (2017). Cloud feedback
940 mechanisms and their representation in global climate models. *Wiley Interdis-
941 cip. Rev. Clim. Chang.*, *8*. doi: 10.1002/wcc.465
942 Chaboureau, J. P., Guichard, F., Redelsperger, J. L., & Lafore, J. P. (2004). The
943 role of stability and moisture in the diurnal cycle of convection over land. *Q.
944 J. R. Meteorol. Soc.*, *130 C*(604), 3105–3117. doi: 10.1256/qj.03.132
945 Choi, Y.-S., Kim, W., Yeh, S.-W., Masunaga, H., Kwon, M.-J., Jo, H.-S., & Huang,
946 L. (2017). Revisiting the iris effect of tropical cirrus clouds with TRMM
947 and A-Train satellite data. *J. Geophys. Res. Atmos.*, *122*, 5917–5931. doi:
948 10.1002/2016JD025827
949 Colman, R. (2003). A comparison of climate feedbacks in general circulation models.
950 *Clim. Dyn.*, *20*(7-8), 865–873. doi: 10.1007/s00382-003-0310-z
951 Dee, D. P., Uppala, S. M., Simmons, A. J., Berrisford, P., Poli, P., Kobayashi, S., ...
952 Vitart, F. (2011). The ERA-Interim reanalysis: Configuration and performance
953 of the data assimilation system. *Q. J. R. Meteorol. Soc.*, *137*(656), 553–597.
954 doi: 10.1002/qj.828
955 Dennis, J. M., Edwards, J., Evans, K. J., Guba, O., Lauritzen, P. H., Mirin, A. A.,
956 ... Worley, P. H. (2012). CAM-SE: A scalable spectral element dynamical
957 core for the Community Atmosphere Model. *Int. J. High Perform. Comput.
958 Appl.*, *26*(1), 74–89. doi: 10.1177/1094342011428142
959 Diffenbaugh, N. S., & Giorgi, F. (2012). Climate change hotspots in the CMIP5
960 global climate model ensemble. *Clim. Change*, *114*(3-4), 813–822. doi: 10
961 .1007/s10584-012-0570-x
962 Fiolleau, T., & Roca, R. (2013). An algorithm for the detection and tracking of
963 tropical mesoscale convective systems using infrared images from geostation-
964 ary satellite. *IEEE Trans. Geosci. Remote Sens.*, *51*(7), 4302–4315. doi:
965 10.1109/TGRS.2012.2227762
966 Fischer, E. M., & Knutti, R. (2015). Anthropogenic contribution to global oc-
967 currence of heavy-precipitation and high-temperature extremes. *Nat. Clim.
968 Chang.*, *5*(6), 560–564. doi: 10.1038/nclimate2617
969 Fischer, E. M., & Knutti, R. (2016). Observed heavy precipitation increase confirms
970 theory and early models. *Nat. Clim. Chang.*, *6*(11), 986–991. Retrieved from
971 `http://www.nature.com/doifinder/10.1038/nclimate3110` doi: 10.1038/
972 nclimate3110
973 Fu, Q., Baker, M., & Hartmann, D. L. (2002). Tropical cirrus and water vapor : an
974 effective Earth infrared iris feedback ? *Atmos. Chem. Phys.*, *2*, 31–37.
975 Gasparini, B., Blossey, P. N., Hartmann, D. L., Lin, G., & Fan, J. (2019). What
976 drives the lifecycle of tropical anvil clouds ? *J. Adv. Model. Earth Syst.*, *11*,
977 2586–2605. doi: 10.1029/2019MS001736
978 Gehlot, S., & Quaas, J. (2012). Convection-climate feedbacks in the ECHAM5
979 general circulation model: Evaluation of cirrus cloud life cycles with ISCCP
980 satellite data from a lagrangian trajectory perspective. *J. Clim.*, *25*(15),

5241–5259. doi: 10.1175/JCLI-D-11-00345.1

Gettelman, A., Liu, X., Ghan, S. J., Morrison, H., Park, S., Conley, a. J., ... Li, J. L. F. (2010). Global simulations of ice nucleation and ice supersaturation with an improved cloud scheme in the Community Atmosphere Model. *J. Geophys. Res. Atmos.*, *115*, 1–19. doi: 10.1029/2009JD013797

Gettelman, A., & Morrison, H. (2015). Advanced two-moment bulk microphysics for global models. Part I: Off-line tests and comparison with other schemes. *J. Clim.*, *28*(3), 1268–1287. doi: 10.1175/JCLI-D-14-00102.1

Golaz, J., Caldwell, P. M., Van Roekel, L. P., Petersen, M. R., Tang, Q., Wolfe, J. D., ... Zhu, Q. (2019). The DOE E3SM coupled model version 1: Overview and evaluation at standard resolution. *J. Adv. Model. Earth Syst.*. doi: 10.1029/2018ms001603

Golaz, J.-C., Larson, V. E., & Cotton, W. R. (2002). A PDF-Based Model for Boundary Layer Clouds. Part I: Method and Model Description. *J. Atmos. Sci.*, *59*(24), 3540–3551. doi: 10.1175/1520-0469(2002)059⟨3540:APBMFB⟩2.0.CO;2

Harrop, B. E., & Hartmann, D. L. (2012). Testing the role of radiation in determining tropical cloud-top temperature. *J. Clim.*, *25*(17), 5731–5747. doi: 10.1175/JCLI-D-11-00445.1

Harrop, B. E., & Hartmann, D. L. (2016). The role of cloud radiative heating within the atmosphere on the high cloud amount and top-of-atmosphere cloud radiative effect. *J. Adv. Model. Earth Syst.*, *8*, 1391–1410. doi: 10.1002/2016MS000670

Hartmann, D. L., & Berry, S. E. (2017). The Balanced Radiative Effect of Tropical Anvil Clouds. *J. Geophys. Res. Atmos.*, *122*. doi: 10.1002/2017JD026460

Hartmann, D. L., Blossey, P. N., & Dygert, B. D. (2019, jun). Convection and Climate: What Have We Learned from Simple Models and Simplified Settings? *Curr. Clim. Chang. Reports*. Retrieved from `https://doi.org/10.1007/s40641-019-00136-9` doi: 10.1007/s40641-019-00136-9

Hartmann, D. L., Dygert, B. D., Fu, Q., & Blossey, P. N. (2020). The Warming Physics of Tropic World : Part 1 Mean State. *J. Adv. Model. Earth Syst.*, 1–27. doi: https://doi.org/10.1002/essoar.10503489.1

Hartmann, D. L., & Larson, K. (2002). An important constraint on tropical cloud - climate feedback. *Geophys. Res. Lett.*, *29*(20), 1951:12. doi: 10.1029/2002GL015835

Hartmann, D. L., & Michelsen, M. L. (2002). No evidence for iris. *BAMS*(February 2002), 249–254.

Hurrell, J. W., Hack, J. J., Shea, D., Caron, J. M., & Rosinski, J. (2008). A new sea surface temperature and sea ice boundary dataset for the community atmosphere model. *J. Clim.*, *21*(19), 5145–5153. doi: 10.1175/2008JCLI2292.1

Iacono, M. J., Delamere, J. S., Mlawer, E. J., Shephard, M. W., Clough, S. A., & Collins, W. D. (2008). Radiative forcing by long-lived greenhouse gases: Calculations with the AER radiative transfer models. *J. Geophys. Res. Atmos.*, *113*(13), 2–9. doi: 10.1029/2008JD009944

Jakob, C., Singh, M. S., & Jungandreas, L. (2019). Radiative Convective Equilibrium and Organized Convection: An Observational Perspective. *J. Geophys. Res. Atmos.*, *124*(10), 5418–5430. doi: 10.1029/2018JD030092

Jensen, E. J., van den Heever, S. C., & Grant, L. D. (2018). The lifecycles of ice crystals detrained from the tops of deep convection. *J. Geophys. Res. Atmos.*, 1–11. Retrieved from `http://doi.wiley.com/10.1029/2018JD028832` doi: 10.1029/2018JD028832

Kato, S., Rose, F. G., Sun-Mack, S., Miller, W. F., Chen, Y., Rutan, D. A., ... Collins, W. D. (2011). Improvements of top-of-atmosphere and surface irradiance computations with CALIPSO-, CloudSat-, and MODIS-derived cloud and aerosol properties. *J. Geophys. Res. Atmos.*, *116*(19), 1–21. doi:

10.1029/2011JD016050

Khairoutdinov, M., & Emanuel, K. (2013). Rotating radiative-convective equilibrium simulated by a cloud-resolving model. *J. Adv. Model. Earth Syst.*, *5*(4), 816–825. doi: 10.1002/2013ms000253

Khairoutdinov, M., & Randall, D. (2006). High-resolution simulation of shallow-to-deep convection transition over land. *J. Atmos. Sci.*, *63*(12), 3421–3436. doi: 10.1175/JAS3810.1

Kiladis, G. N., Wheeler, M. C., Haertel, P. T., Straub, K. H., & Roundy5, P. E. (2009). Convectively Coupled Equatorial Waves. *Rev. Geophys.*, *47*(RG2003), 1–22. doi: 10.1029/2008RG000266.1.HISTORICAL

Klein, S. a., & Jakob, C. (1999). Validation and Sensitivities of Frontal Clouds Simulated by the ECMWF Model. *Mon. Weather Rev.*, *127*(10), 2514–2531. doi: 10.1175/1520-0493(1999)127⟨2514:VASOFC⟩2.0.CO;2

Kuang, Z., & Bretherton, C. S. (2006). A mass-flux scheme view of a high-resolution simulation of a transition from shallow to deep cumulus convection. *J. Atmos. Sci.*, *63*(7), 1895–1909. doi: 10.1175/JAS3723.1

Kuang, Z., & Hartmann, D. L. (2007). Testing the fixed anvil temperature hypothesis in a cloud-resolving model. *J. Clim.*, *20*(10), 2051–2057. doi: 10.1175/JCLI4124.1

Kubar, T. L., Hartmann, D. L., & Wood, R. (2007). Radiative and convective driving of tropical high clouds. *J. Clim.*, *20*(22), 5510–5526. doi: 10.1175/2007JCLI1628.1

Larson, V. E., & Golaz, J.-C. (2005). Using Probability Density Functions to Derive Consistent Closure Relationships among Higher-Order Moments. *Mon. Weather Rev.*, *133*(4), 1023–1042. doi: 10.1175/MWR2902.1

Lindzen, R. S., & Choi, Y. S. (2011). On the observational determination of climate sensitivity and its implications. *Asia-Pacific J. Atmos. Sci.*, *47*(4), 377–390. doi: 10.1007/s13143-011-0023-x

Lindzen, R. S., Chou, M. D., & Hou, A. Y. (2001). Does the Earth Have an Adaptive Infrared Iris? *Bull. Am. Meteorol. Soc.*, *82*(3), 417–432. doi: 10.1175/1520-0477(2002)083⟨0597:CODTEH⟩2.3.CO;2

Lohmann, U., Lüond, F., & Mahrt, F. (2016). *An introduction to clouds: From the microscale to climate*. Cambridge University Press.

Luo, Z., & Rossow, W. B. (2004). Characterizing Tropical Cirrus Life Cycle, Evolution, and Interaction with Upper-Tropospheric Water Vapor Using Lagrangian Trajectory Analysis of Satellite Observations. *J. Clim.*, *17*, 4541–4563. Retrieved from `http://journals.ametsoc.org/doi/pdf/10.1175/3222.1` doi: 10.1175/3222.1

Mace, G. G., & Berry, E. (2017). Using Active Remote Sensing to Evaluate Cloud-Climate Feedbacks: a Review and a Look to the Future. *Curr. Clim. Chang. Reports*, *819*. Retrieved from `http://link.springer.com/10.1007/s40641-017-0067-9` doi: 10.1007/s40641-017-0067-9

Mace, G. G., Deng, M., Soden, B., & Zipser, E. (2006). Association of Tropical Cirrus in the 10–15-km Layer with Deep Convective Sources: An Observational Study Combining Millimeter Radar Data and Satellite-Derived Trajectories. *J. Atmos. Sci.*, *63*(2), 480–503. doi: 10.1175/JAS3627.1

Machado, L. A., Rossow, W. B., Guedes, R. L., & Walker, A. W. (1998). Life cycle variations of mesoscale convective systems over the Americas. *Mon. Weather Rev.*, *126*(6), 1630–1654. doi: 10.1175/1520-0493(1998)126⟨1630:LCVOMC⟩2.0.CO;2

Mapes, B. E., & Houze, R. A. (1993). Cloud clusters and superclusters over the oceanic warm pool. *Mon. Weather Rev.*, *121*(5), 1398–1415. doi: 10.1175/1520-0493(1993)121⟨1398:ccasot⟩2.0.co;2

Marvel, K., Zelinka, M., Klein, S. A., Bonfils, C., Caldwell, P., Doutriaux, C., ... Taylor, K. E. (2015). External influences on modeled and observed cloud

trends. *J. Clim.*, *28*(12), 4820–4840. doi: 10.1175/JCLI-D-14-00734.1

Mauritsen, T., & Stevens, B. (2015). Missing iris effect as a possible cause of muted hydrological change and high climate sensitivity in models. *Nat. Geosci.*, *8*(5), 346–351. Retrieved from `http://www.nature.com/doifinder/10.1038/ngeo2414` doi: 10.1038/ngeo2414

Meyers, M. P., Demott, P. J., & Cotton, W. R. (1992). New primary ice-nucleation parameterizations in an explicit cloud model. *J. Appl. Meteorol.*, *31*(7), 708–721. doi: 10.1175/1520-0450(1992)031⟨0708:NPINPI⟩2.0.CO;2

Miltenberger, A. K., Pfahl, S., & Wernli, H. (2013). An online trajectory module (version 1.0) for the nonhydrostatic numerical weather prediction model COSMO. *Geosci. Model Dev.*, *6*(6), 1989–2004. doi: 10.5194/gmd-6-1989-2013

Mlawer, E. J., Taubman, J., Brown, P. D., Iacono, M. J., & Clough, S. A. (1997). Radiative transfer for inhomogeneous atmospheres: RRTM, a validated correlatedk model for the longwave. *J. Geophys. Res.*, *102*(D14), 16663–16682. doi: doi:10.1029/97JD00237

Morrison, H., & Gettelman, A. (2008). A new two-moment bulk stratiform cloud microphysics scheme in the community atmosphere model, version 3 (CAM3). Part I: Description and numerical tests. *J. Clim.*, *21*(15), 3642–3659. doi: 10.1175/2008JCLI2105.1

Neale, R. B., Gettelman, A., Park, S., Chen, C.-c., Lauritzen, P. H., Williamson, D. L., ... Taylor, M. A. (2012). *Description of the NCAR Community Atmosphere Model (CAM 5.0)* (Tech. Rep. No. November). NCAR.

Neale, R. B., Richter, J. H., & Jochum, M. (2008). The impact of convection on ENSO: From a delayed oscillator to a series of events. *J. Clim.*, *21*(22), 5904–5924. doi: 10.1175/2008JCLI2244.1

Nesbitt, S. W., & Zipser, E. J. (2003). The Diurnal Cycle of Rainfall and Convective Intensity according to Three Years of TRMM Measurements. *J. Clim.*, *16*(10), 1456–1475. doi: 10.1175/1520-0442-16.10.1456

Norris, J. R., Allen, R. J., Evan, A. T., Zelinka, M. D., O'Dell, C. W., & Klein, S. A. (2016). Evidence for climate change in the satellite cloud record. *Nature*, *536*(7614), 72–75. Retrieved from `http://dx.doi.org/10.1038/nature18273` doi: 10.1038/NATURE18273

Ohno, T., & Satoh, M. (2018). Roles of Cloud Microphysics on Cloud Responses to Sea Surface Temperatures in Radiative-Convective Equilibrium Experiments Using a High-Resolution Global Nonhydrostatic Model. *J. Adv. Model. Earth Syst.*, *10*, 1970–1989. doi: 10.1029/2018MS001386

Ohno, T., Satoh, M., & Noda, A. (2019). Fine vertical resolution Radiative-Convective Equilibrium Experiments: roles of turbulent mixing on the High-Cloud Response to Sea Surface Temperatures. *J. Adv. Model. Earth Syst.*, *11*, 1–18. doi: 10.1029/2019ms001704

Pendergrass, A. G., & Knutti, R. (2018). The Uneven Nature of Daily Precipitation and Its Change. *Geophys. Res. Lett.*, *45*(21), 11,980–11,988. doi: 10.1029/2018GL080298

Prein, A. F., Liu, C., Ikeda, K., Trier, S. B., Rasmussen, R. M., Holland, G. J., & Clark, M. P. (2017). Increased rainfall volume from future convective storms in the US. *Nat. Clim. Chang.*, *7*(12), 880–884. Retrieved from `http://dx.doi.org/10.1038/s41558-017-0007-7` doi: 10.1038/s41558-017-0007-7

Protopapadaki, S. E., Stubenrauch, C. J., & Feofilov, A. G. (2017). Upper Tropospheric Cloud Systems Derived from IR Sounders: Properties of Cirrus Anvils in the Tropics. *Atmos. Chem. Phys.*, *17*, 3845–3859. Retrieved from `www.atmos-chem-phys.net/17/3845/2017/` doi: 10.5194/acp-17-3845-2017

Rasch, P. J., Xie, S., Ma, P.-l., Lin, W., Wang, H., Tang, Q., & Burrows, S. M. (2019). An Overview of the Atmospheric Component of the Energy Exascale Earth System Model. *J. Adv. Model. Earth Syst.*, *11*(8), 2377–2411. doi:

https://doi.org/10.1029/2019MS001629Received

Rempel, M., Senf, F., & Deneke, H. (2017). Object-based metrics for forecast verification of convective development with geostationary satellite data. *Mon. Weather Rev.*, *145*(8), 3161–3178. doi: 10.1175/MWR-D-16-0480.1

Roca, R., Fiolleau, T., & Bouniol, D. (2017). A simple model of the life cycle of mesoscale convective systems cloud shield in the tropics. *J. Clim.*, *30*(11), 4283–4298. doi: 10.1175/JCLI-D-16-0556.1

Satoh, M., Iga, S. I., Tomita, H., Tsushima, Y., & Noda, A. T. (2011). Response of Upper Clouds in Global Warming Experiments Obtained Using a Global Nonhydrostatic Model with Explicit Cloud Processes. *J. Clim.*, *25*, 2178–2191. doi: 10.1175/JCLI-D-11-00152.1

Seeley, J. T., & Romps, D. M. (2015). Why does tropical convective available potential energy (CAPE) increase with warming? *Geophys. Res. Lett.*, *42*(23), 10429–10437. doi: 10.1002/2015GL066199

Senf, F., Klocke, D., & Brueck, M. (2018). Size-resolved evaluation of simulated deep tropical convection. *Mon. Weather Rev.*, *146*(7), 2161–2182. doi: 10.1175/MWR-D-17-0378.1

Soden, B. J., Broccoli, A. J., & Hemler, R. S. (2004). On the use of cloud forcing to estimate cloud feedback. *J. Clim.*, *17*(19), 3661–3665. doi: 10.1175/1520-0442(2004)017⟨3661:OTUOCF⟩2.0.CO;2

Soden, B. J., Held, I. M., Colman, R. C., Shell, K. M., Kiehl, J. T., & Shields, C. A. (2008). Quantifying climate feedbacks using radiative kernels. *J. Clim.*, *21*(14), 3504–3520. doi: 10.1175/2007JCLI2110.1

Sprenger, M., & Wernli, H. (2015). The LAGRANTO Lagrangian analysis tool – version 2.0. *Geosci. Model Dev.*, *8*(8), 2569–2586. doi: 10.5194/gmd-8-2569-2015

Strandgren, J. (2018). *The life cycle of anvil cirrus clouds from a combination of passive and active satellite remote sensing* (PhD Dissertation, LMU Munich). Retrieved from `http://nbn-resolving.de/urn:nbn:de:bvb:19-227892`

Sun, J., Zhang, K., Wan, H., Ma, P. L., Tang, Q., & Zhang, S. (2019). Impact of Nudging Strategy on the Climate Representativeness and Hindcast Skill of Constrained EAMv1 Simulations. *J. Adv. Model. Earth Syst.*, *11*(12), 3911–3933. doi: 10.1029/2019MS001831

Tompkins, A. M., & Craig, G. C. (1999). Sensitivity of tropical convection to sea surface temperature in the absence of large-scale flow. *J. Clim.*, *12*(2), 462–476. doi: 10.1175/1520-0442(1999)012⟨0462:SOTCTS⟩2.0.CO;2

Tsushima, Y., Iga, S. I., Tomita, H., Satoh, M., Noda, A. T., & Webb, M. J. (2015). High cloud increase in a perturbed SST experiment with a global nonhydrostatic model including explicit convective processes. *J. Adv. Model. Earth Syst.*, *6*(3), 571–585. doi: 10.1002/2013MS000301

Van Diedenhoven, B., Fridlind, A. M., Cairns, B., Ackerman, A. S., & Yorks, J. E. (2016). Vertical variation of ice particle size in convective cloud tops. *Geophys. Res. Lett.*, *43*(9), 4586–4593. doi: 10.1002/2016GL068548

van Diedenhoven, B., Ackerman, A. S., Fridlind, A. M., Cairns, B., & Riedi, J. (2020). Global Statistics of Ice Microphysical and Optical Properties at Tops of Optically Thick Ice Clouds. *J. Geophys. Res. Atmos.*, *125*(6), 1–21. doi: 10.1029/2019JD031811

Wall, C. J., & Hartmann, D. L. (2018). Balanced Cloud Radiative Effects Across a Range of Dynamical Conditions Over the Tropical West Pacific. *Geophys. Res. Lett.*, *5*, 490–498. doi: 10.1029/2018GL080046

Wall, C. J., Hartmann, D. L., Thieman, M. M., Smith, W. L., & Minnis, P. (2018). The Life Cycle of Anvil Clouds and the Top-of-Atmosphere Radiation Balance over the Tropical West Pacific. *J. Clim.*, *31*(24), 10059–10080. Retrieved from `http://journals.ametsoc.org/doi/10.1175/JCLI-D-18-0154.1` doi: 10.1175/JCLI-D-18-0154.1

Wang, M., & Zhang, G. J. (2018). Improving the simulation of tropical convective cloud-top heights in CAM5 with CloudSat observations. *J. Clim.*, *31*(13), 5189–5204. doi: 10.1175/JCLI-D-18-0027.1

Webb, M., Senior, C., Bony, S., & Morcrette, J. J. (2001). Combining ERBE and ISCCP data to assess clouds in the Hadley Centre, ECMWF and LMD atmospheric climate models. *Clim. Dyn.*, *17*(12), 905–922. doi: 10.1007/s003820100157

Wernli, H., & Davies, H. C. (1997). A Lagrangian-based analysis of extratropical cyclones .1. The method and some applications. *Q. J. R. Meteorol. Soc.*, *123*(538), 467–489. doi: 10.1256/smsqj.53810

Wielicki, B. A., Barkstrom, B. R., Harrison, E. F., Lee, R. B., Smith, G. L., & Cooper, J. E. (1996). Clouds and the Earth's Radiant Energy System (CERES): An Earth Observing System Experiment. *Bull. Am. Meteorol. Soc.*, *77*(5), 853–868. doi: 10.1175/1520-0477(1996)077⟨0853:CATERE⟩2.0.CO;2

Wing, A., Stauffer, C., Reed, K., Becker, T., Satoh, M., Stevens, B., ... Ohno, T. (2019). *Tropical clouds and convection in RCE simulations.* Mykonos, Greece.

Xie, S., Lin, W., Rasch, P. J., Ma, P.-L., Neale, R., Larson, V. E., ... Zhang, Y. (2018). Understanding Cloud and Convective Characteristics in Version 1 of the E3SM Atmosphere Model. *J. Adv. Model. Earth Syst.*, *0*, 1–27. Retrieved from `http://doi.wiley.com/10.1029/2018MS001350` doi: 10.1029/2018MS001350

Yoshimori, M., Lambert, F. H., Webb, M. J., & Andrews, T. (2020). Fixed Anvil Temperature Feedback: Positive, Zero, or Negative? *J. Clim.*, *33*(7), 2719–2739. doi: 10.1175/jcli-d-19-0108.1

Zelinka, M. D., & Hartmann, D. L. (2010). Why is longwave cloud feedback positive? *J. Geophys. Res. Atmos.*, *115*(16), 1–16. doi: 10.1029/2010JD013817

Zelinka, M. D., Klein, S. A., & Hartmann, D. L. (2012a). Computing and partitioning cloud feedbacks using cloud property histograms. Part I: Cloud radiative kernels. *J. Clim.*, *25*(11), 3715–3735. doi: 10.1175/JCLI-D-11-00248.1

Zelinka, M. D., Klein, S. A., & Hartmann, D. L. (2012b). Computing and Partitioning Cloud Feedbacks Using Cloud Property Histograms . Part II : Attribution to Changes in Cloud Amount , Altitude , and Optical Depth. *J. Clim.*, *25*, 3736–3754. doi: 10.1175/JCLI-D-11-00249.1

Zelinka, M. D., Klein, S. A., Taylor, K. E., Andrews, T., Webb, M. J., Gregory, J. M., & Forster, P. M. (2013). Contributions of different cloud types to feedbacks and rapid adjustments in CMIP5. *J. Clim.*, *26*(14), 5007–5027. doi: 10.1175/JCLI-D-12-00555.1

Zelinka, M. D., Zhou, C., & Klein, S. A. (2016). Insights from a Refined Decomposition of Cloud Feedbacks. *Geophys. Res. Lett.*, *43*. doi: 10.1002/2016GL069917

Zhang, G. J., & McFarlane, N. A. (1995). Sensitivity of climate simulations to the parameterization of cumulus convection in the canadian climate centre general circulation model. *Atmos. - Ocean*, *33*(3), 407–446. doi: 10.1080/07055900.1995.9649539

Zhang, Y., Xie, S., Lin, W., Klein, S. A., Zelinka, M., Ma, P. L., ... Ma, H. Y. (2019). Evaluation of Clouds in Version 1 of the E3SM Atmosphere Model With Satellite Simulators. *J. Adv. Model. Earth Syst.*, 1–16. doi: 10.1029/2018MS001562

Zhao, X., Lin, Y., Peng, Y., Wang, B., Morrison, H., & Gettelman, A. (2017). A single ice approach using varying ice particle properties in global climate model microphysics. *J. Adv. Model. Earth Syst.*, *9*(5), 2138–2157. doi: 10.1002/2017MS000952

Zhou, C., Dessler, A., Zelinka, M., Yang, P., & Wang, T. (2014). Cirrus feedback on interannual climate fluctuations. *Geophys. Res. Lett*, *41*, 9166–9173. doi: 10.1002/2013GL058954.Received